

## SPECTRAL FORMATION IN X-RAY PULSARS: BULK COMPTONIZATION IN THE ACCRETION SHOCK

PETER A. BECKER

Center for Earth Observing and Space Research and Department of Physics and Astronomy, George Mason University,  
4400 University Drive, Fairfax, VA 22030-4444; pbecker@gmu.edu

AND

MICHAEL T. WOLFF

E. O. Hulburt Center for Space Research, Naval Research Laboratory, Washington, DC 20375; michael.wolff@nrl.navy.mil

Received 2005 February 2; accepted 2005 May 4

### ABSTRACT

Accretion-powered X-ray pulsars are among the most luminous X-ray sources in the Galaxy. However, despite decades of theoretical and observational work since their discovery, no satisfactory model for the formation of the observed X-ray spectra has emerged. In particular, the previously available theories are unable to reproduce the power-law variation observed at high energies in many sources. In this paper we present the first self-consistent calculation of the spectrum emerging from a pulsar accretion column that includes an explicit treatment of the energization occurring in the shock. Using a rigorous eigenfunction expansion method based on the exact dynamical solution for the velocity profile in the column, we obtain a closed-form expression for the Green's function describing the upscattering of radiation injected into the column from a monochromatic source located at the top of the thermal mound, near the base of the flow. The Green's function is convolved with a Planck distribution to calculate the radiation spectrum resulting from the reprocessing of blackbody photons emitted by the thermal mound. We demonstrate that the energization of the photons in the shock naturally produces an X-ray spectrum with a power-law shape at high energies and a blackbody shape at low energies, in agreement with many observations of accreting X-ray pulsars.

*Subject headings:* methods: analytical — pulsars: general — radiation mechanisms: nonthermal — shock waves — stars: neutron — X-rays: stars

### 1. INTRODUCTION

Since the discovery of the first known pulsating X-ray sources Her X-1 and Cen X-3 more than three decades ago (Giacconi et al. 1971; Tananbaum et al. 1972), over 50 new sources have been detected in the Galaxy and the Magellanic Clouds, with luminosities in the range  $L_X \sim 10^{34} - 10^{38}$  ergs  $s^{-1}$  and pulsation periods  $0.1 \text{ s} \lesssim P \lesssim 10^3 \text{ s}$ . X-ray pulsars include a variety of objects powered by rotation or accretion, as well as several anomalous X-ray pulsars whose energy source is currently unclear. The emission from X-ray pulsars in binary systems is fueled by the accretion of material from the “normal” companion onto the neutron star, with the flow channeled onto one or both of the magnetic poles by the strong field. During the accretion process, gravitational potential energy is converted into kinetic energy, which escapes from the column in the form of X-rays as the gas decelerates through a radiative shock before settling onto the stellar surface. In the accretion-powered sources, which are the focus of this paper, the X-ray spectra are often well fitted using a combination of a power-law spectrum plus a blackbody component with a temperature in the range  $T \sim 10^6 - 10^7$  K (e.g., Coburn et al. 2002; di Salvo et al. 1998; White et al. 1983). Most spectra also display quasi-exponential cutoffs at  $E \sim 20 - 30$  keV, and there are indications of cyclotron features and iron emission lines in a number of sources. The observations suggest typical magnetic field strengths of  $\sim 10^{12} - 10^{13}$  G.

Although accretion-powered X-ray pulsars are among the most luminous sources in the Galaxy, previous attempts to calculate their spectra based on static or dynamic theoretical models have generally yielded results that do not agree very well with the observed profiles (e.g., Mészáros & Nagel 1985a, 1985b; Nagel 1981; Yahel 1980; Klein et al. 1996). Hence, there is still

no clear understanding of the basic spectral formation mechanism in X-ray pulsars (see the discussion in Coburn et al. 2002). Given the lack of a viable theoretical model, X-ray pulsar spectral data have traditionally been fitted using multicomponent forms that include absorbed power laws, cyclotron features, iron emission lines, blackbody components, and high-energy exponential cutoffs. The resulting parameters are sometimes difficult to relate to the physical properties of the source. Motivated by the lack of a comprehensive theoretical model for X-ray pulsar spectral formation, we reconsider here the physical picture originally proposed by Davidson (1973), in which the accreting gas passes through a radiative, radiation-dominated shock before settling onto the surface of the star. We illustrate the accretion/emission geometry schematically in Figure 1. Most of the photons emitted from the accretion column are produced in the dense “thermal mound” located inside the column, just above the stellar surface. The blackbody photons created in the mound are upscattered in the shock and eventually diffuse through the walls of the column. The escaping photons carry away the kinetic energy of the gas, thereby allowing the plasma to settle onto the surface of the star. Hence, the formation of the emergent spectrum is intimately connected with the dynamics of the accreting gas.

#### 1.1. Bulk Comptonization

The strong compression that occurs as the plasma crosses the radiative shock renders it an ideal site for first-order Fermi energization (i.e., “bulk” or “dynamical” Comptonization) of the photons produced by the thermal mound. In the bulk Comptonization process, particles experience a mean energy gain if the scattering centers they collide with are involved in a

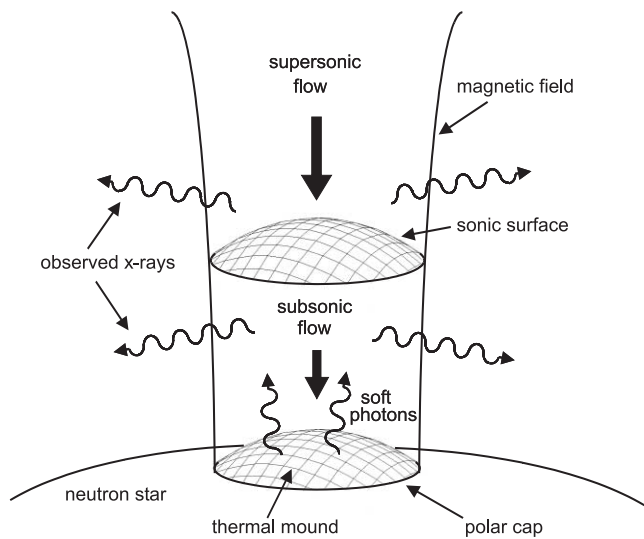


FIG. 1.—Schematic depiction of gas accreting onto one of the magnetic polar caps of a neutron star.

converging flow (e.g., Laurent & Titarchuk 1999; Turolla et al. 2002). By contrast, in the thermal Comptonization process, particles gain energy due to the *stochastic* motions of the scattering centers via the second-order Fermi mechanism (e.g., Sunyaev & Titarchuk 1980; Becker 2003). In the X-ray pulsar application, the scattering centers are infalling electrons, and the energized “particles” are photons. Since the inflow speed of the electrons in an X-ray pulsar accretion column is much larger than their thermal velocity, bulk Comptonization dominates over the stochastic process except at the highest photon energies (Titarchuk et al. 1996), as discussed in § 7. The failure of the current models to generate the power-law spectral shape characteristic of X-ray pulsars probably stems from the neglect of the critical contribution of the shock in upscattering the soft radiation produced in the thermal mound (e.g., Burnard et al. 1991). We demonstrate in this paper that bulk Comptonization of the radiation in the accretion shock can produce spectra very similar to the power-law continuum seen in many X-ray pulsars. The main results presented here were summarized by Becker & Wolff (2005).

Dynamical Comptonization has been considered by a number of previous authors in a variety of astrophysical situations, including spherical inflows (Payne & Blandford 1981; Colpi 1988; Schneider & Bogdan 1989; Titarchuk et al. 1997), accretion disks around black holes (Laurent & Titarchuk 2001; Titarchuk et al. 2002; Titarchuk & Shrader 2002), spherical outflows (Becker & Begelman 1986; Titarchuk et al. 2003), and the transport of cosmic rays in the solar wind (Parker 1965; Stawicki et al. 2000). The process was also studied in the context of neutron star accretion by Titarchuk et al. (1996) and Mastichiadis & Kylafis (1992), although their results are not applicable to X-ray pulsar accretion columns due to the assumption of spherical symmetry and the imposition of a power-law velocity profile. Lyubarskii & Sunyaev (1982) analyzed dynamical Comptonization in the context of plane-parallel pulsar shocks, but the velocity profile they utilized is not consistent with the dynamics of X-ray pulsar accretion, and furthermore they did not account for the escape of radiation through the walls of the column. The relevance of the bulk Comptonization process for spectral formation in X-ray pulsars was also recognized by Burnard et al. (1991), who pointed out

that thermal spectra alone are much too soft to explain the observed emission and suggested that upscattering in the shock could provide the required hardening.

The fundamental character of the Green’s function describing both thermal and bulk Comptonization was studied by Titarchuk & Zannias (1998) for the case of accretion onto a black hole. These authors established that the Green’s function can be approximated using a broken power-law form with a central peak between the high- and low-energy portions of the spectrum, for either type of Comptonization. Furthermore, they concluded that bulk Comptonization dominates over the thermal process if the electron temperature  $T \lesssim 10^7$  K. The theory developed in the present paper represents an extension of the same idea to neutron star accretion, resulting in the exact Green’s function for the X-ray pulsar spectral formation process. In agreement with Titarchuk & Zannias (1998), we find that the bulk Comptonization process is dominant for the temperature range relevant for X-ray pulsars. However, the presence of the event horizon in the black hole application treated by these authors makes their problem fundamentally different from the neutron star accretion problem studied here because the neutron star obviously possesses a solid surface. Our work therefore represents the first exact, quantitative analysis of the role of bulk Comptonization in the X-ray pulsar spectral formation process.

## 1.2. Radiation-dominated Flow

Radiation pressure governs the dynamical structure of the accretion flows in bright pulsars when the X-ray luminosity satisfies (Becker 1998; Basko & Sunyaev 1976)

$$L_X \sim L_{\text{crit}} \equiv \frac{2.72 \times 10^{37} \sigma_T}{\sqrt{\sigma_{\perp} \sigma_{\parallel}}} \left( \frac{M_*}{M_{\odot}} \right) \left( \frac{r_0}{R_*} \right) \text{ ergs s}^{-1}, \quad (1)$$

where  $r_0$  is the polar cap radius,  $M_*$  and  $R_*$  denote the stellar mass and radius, respectively,  $\sigma_T$  is the Thomson cross section, and  $\sigma_{\parallel}$  and  $\sigma_{\perp}$  represent the electron scattering cross sections for photons propagating parallel or perpendicular to the magnetic field, respectively. When the luminosity of the system is comparable to  $L_{\text{crit}}$ , the radiation flux in the column is super-Eddington and therefore the radiation pressure greatly exceeds the gas pressure (Becker 1998). In this situation the gas passes through a radiation-dominated shock on its way to the stellar surface, and the kinetic energy of the gas is carried away by the high-energy radiation that escapes from the column. The strong gradient of the radiation pressure decelerates the material to rest at the surface of the star. The observation of many X-ray pulsars with  $L_X \sim 10^{36} - 10^{38}$  ergs s $^{-1}$  implies the presence of radiation-dominated shocks close to the stellar surfaces in these systems (White et al. 1983, 1995). Note that radiation-dominated shocks are *continuous* velocity transitions, with an overall thickness of a few Thomson scattering lengths, unlike traditional (discontinuous) gas-dominated shocks (Blandford & Payne 1981b).

In luminous X-ray pulsars, the pressure of the radiation determines the dynamics of the flow, while the dynamics in turn determines the shape of the radiation spectrum. Hence, the flow dynamics and the radiative transport are coupled, which makes this a complex and nonlinear “photohydrodynamical” problem. One implication is that the photons scattering through the column cannot be regarded as “test particles” since it is their pressure that dictates the structure of the flow. We must therefore solve for the radiation spectrum and the velocity profile in a self-consistent manner. Radiation pressure may also play an

important role in the dynamics of moderate-luminosity pulsars due to the strong dependence of the electron scattering (cyclotron) cross section on the magnetic field strength (Langer & Rappaport 1982).

Becker (1998) and Basko & Sunyaev (1976) have considered the dynamics of radiation-dominated pulsar accretion flows, including the effect of the shock and the escape of radiation energy from the column. They find that the gas is decelerated to zero velocity in a manner consistent with accretion onto a solid body, but they do not consider the shape of the escaping radiation spectrum. Conversely, the dynamics and the radiation spectrum have been worked out self-consistently by Blandford & Payne (1981b) for the case of a “standard” (Rankine-Hugoniot) radiation-dominated shock, which does not include radiation escape. In the Blandford & Payne (1981b) approach, the radiation spectrum everywhere in the flow is determined by solving the transport equation using the incident radiation field as a boundary condition. The solutions have a power-law character at high energies, with a spectral index that depends on the Mach number of the upstream flow. Since the Rankine-Hugoniot shocks studied by Blandford & Payne (1981b) have a conserved energy flux, the downstream velocity is never less than one-seventh its upstream value. Consequently, the associated spectral solutions are not applicable to the X-ray pulsar case, since pulsar shocks must be *radiative* in nature so that the kinetic energy of the infalling material can be removed and the flow brought to rest at the stellar surface.

The analytical approach employed here parallels the work of Blandford & Payne (1981b), except that the velocity profile they utilized is replaced with the appropriate solution for an X-ray pulsar accretion column, and the loss of radiation energy from the column is incorporated into the transport equation using an escape probability formalism. In the spirit of the Blandford & Payne (1981b) study of spectral formation in radiation-dominated Rankine-Hugoniot shocks, we are interested here in exploring the direct effect of the radiative accretion shock on the spectrum emerging from an X-ray pulsar. Hence, it is not our goal in this paper to develop complete models that include additional processes such as free-free emission and absorption, cyclotron features, and iron emission lines. However, even without including any of these processes, we are able to demonstrate qualitative agreement with X-ray pulsar spectra. This suggests that energization in the accretion shock is one of the most important aspects of spectral formation in X-ray pulsars.

The remainder of the paper is organized as follows. In § 2 we briefly review the conservation equations and discuss the resulting dynamical solution for the velocity profile of the accreting gas. The transport equation governing the scattering of the radiation inside the accretion column is analyzed in § 3, and various constraints are derived in order to ensure that the radiative transfer is modeled in a manner consistent with the flow dynamics. In § 4 we obtain the exact analytical solution for the Green’s function and convolve it with the Planck distribution emitted at the thermal mound to compute the radiation spectrum emerging from the accretion column. In § 5 we present results obtained for the count rate spectra using parameters corresponding to specific pulsars, and we compare the theoretical spectra with the observational data. The implications of our results for the production of X-ray spectra in pulsars are discussed in § 7. Additional mathematical details are provided in a series of appendices.

## 2. DYNAMICS OF RADIATION-DOMINATED FLOW

The model analyzed here is based on the dynamical picture suggested by Davidson (1973), which is illustrated schemati-

cally in Figure 1. The accretion scenario corresponds physically to the flow of a mixture of gas and radiation inside a magnetic “pipe” that is sealed with respect to the gas but is transparent with respect to the radiation. The accretion column incorporates a radiation-dominated, radiative shock located above the stellar surface. Although the shock is extended and the velocity profile is continuous, the flow possesses a well-defined sonic surface, as indicated in Figure 1. The model also includes a dense thermal mound located at the base of the flow, where local thermodynamic equilibrium prevails. Due to its blackbody nature, the thermal mound acts as both a photon source (emitting a Planck spectrum) and a photon sink (absorbing all incident radiation). Hence, the surface of the mound represents the “photosphere” for photon creation and absorption, and the opacity is dominated by electron scattering above this point.

In our approach to the problem, we assume that the upstream flow is composed of pure, fully ionized hydrogen gas moving at a highly supersonic speed, which is the standard scenario for accretion-powered X-ray pulsars (Basko & Sunyaev 1975, 1976). Our transport model employs a cylindrical, plane-parallel geometry, and therefore the velocity, density, and pressure are functions of the distance above the stellar surface, but they are all constant across the column at a given height. In this situation, the vertical variation of the flow velocity is given by the exact analytical solution obtained by Becker (1998) and Basko & Sunyaev (1976), which describes the settling of the transonic flow onto the surface of the star. A detailed consideration of the angular and energy dependencies of the electron scattering cross section is beyond the scope of the present paper. We therefore follow Wang & Frank (1981) and Becker (1998) by treating the directional dependence of the electron scattering in an approximate way in terms of the energy-averaged cross sections  $\sigma_{\parallel}$  and  $\sigma_{\perp}$ , describing, respectively, the scattering of photons propagating either parallel or perpendicular to the magnetic field. The gas in the accretion column is radiation dominated, and therefore it is the pressure of the photons that decelerates the infalling plasma to rest. We use this fact in § 6.1 to evaluate the self-consistency of the coupled radiative transport/dynamical model based on the analytical solution for the radiation pressure profile obtained below.

### 2.1. Conservation Equations

The one-dimensional, time-dependent Euler equations governing the flow of a radiation-dominated gas with mass density  $\rho$ , flow velocity  $v$ , and photon energy density  $U$  inside a cylindrical accretion column are

$$\frac{\partial \rho}{\partial t} = -\frac{\partial J}{\partial x}, \quad (2)$$

$$\frac{\partial}{\partial t}(\rho v) = -\frac{\partial I}{\partial x}, \quad (3)$$

$$\frac{\partial}{\partial t} \left( \frac{1}{2} \rho v^2 + U \right) = -\frac{\partial E}{\partial x} + \dot{U}_{\text{esc}} + \dot{U}_{\text{abs}} + \dot{U}_{\text{emit}}, \quad (4)$$

where the mass, momentum, and energy fluxes are given, respectively, by

$$J = \rho v, \quad (5)$$

$$I = P + \rho v^2, \quad (6)$$

$$E = \frac{1}{2} \rho v^3 + P v + U v - c \frac{\partial P}{\partial \tau_{\parallel}}, \quad (7)$$

with  $P = U/3$  denoting the radiation pressure. The spatial coordinate  $x$  increases along the column axis, in the direction of the flow, and  $\tau_{\parallel}$  denotes the associated electron scattering optical depth, which is related to  $x$  via

$$d\tau_{\parallel} = n_e \sigma_{\parallel} dx, \quad (8)$$

where  $n_e = \rho/m_p$  is the electron number density and  $m_p$  is the proton mass. The two coordinates  $x$  and  $\tau_{\parallel}$  are calibrated so that they each vanish at the sonic point, as explained below.

The quantities  $\dot{U}_{\text{esc}}$ ,  $\dot{U}_{\text{abs}}$ , and  $\dot{U}_{\text{emit}}$  appearing in equation (4) represent the rates per unit volume at which radiation energy escapes through the column walls or is absorbed or emitted by the gas, respectively. When the system is radiation dominated as assumed here, the gas itself has little thermal energy to contribute to the radiation field, although it does possess a large reservoir of *bulk* kinetic energy that is transferred to the photons through the first-order Fermi energization process in the shock. In this situation, the emission and absorption processes must nearly balance throughout the flow, and therefore we can write

$$\dot{U}_{\text{abs}} + \dot{U}_{\text{emit}} = 0, \quad (9)$$

in which case equation (4) reduces in a steady state to

$$\frac{\partial E}{\partial x} = \dot{U}_{\text{esc}}. \quad (10)$$

Although emission and absorption do not affect the flow dynamics in this situation, these processes profoundly influence the *shape* of the radiation spectrum, as discussed in §§ 3 and 4.

Within the context of our one-dimensional picture, the rate at which radiation energy diffuses through the walls of the column can be approximated using an escape probability formalism. If the column cross section is optically thick to electron scattering, as expected, then the rate at which radiation energy escapes through the walls is given by

$$\dot{U}_{\text{esc}} = -\frac{U}{t_{\text{esc}}}, \quad (11)$$

where the mean escape time,  $t_{\text{esc}}$ , is given by

$$t_{\text{esc}} = \frac{r_0}{w_{\perp}}, \quad w_{\perp} = \frac{c}{\tau_{\perp}}, \quad \tau_{\perp} = n_e \sigma_{\perp} r_0, \quad (12)$$

with  $w_{\perp}$  denoting the diffusion velocity perpendicular to the  $x$ -axis and  $\tau_{\perp}$  representing the perpendicular scattering optical thickness of the cylindrical accretion column with radius  $r_0$ . Note that  $\tau_{\perp}$  and  $t_{\text{esc}}$  are functions of  $x$  through their dependence on  $n_e$ . Becker (1998) confirmed that the diffusion approximation employed in equation (11) is valid because  $\tau_{\perp} > 1$  for typical X-ray pulsar parameters. Equations (5) and (12) can be combined to express the mean escape time as

$$t_{\text{esc}} = \frac{J r_0^2 \sigma_{\perp}}{m_p c v}. \quad (13)$$

Since the escape timescale is inversely proportional to the flow velocity, the column becomes completely opaque at the surface of the neutron star due to the divergence of the electron number

density there. The relationship between the escape probability approximation and the physical distribution of radiation inside the accretion column is further discussed in § 6.3.

## 2.2. Dynamical Solution

In the steady state situation of interest here, the mass flux  $J$  and the momentum flux  $I$  are both conserved, but the energy flux  $E$  decreases as the gas accretes onto the surface of the neutron star due to the emission of radiation through the column walls. The momentum, energy, and mass conservation equations can be combined in this case to show that the flow velocity  $v$  satisfies the second-order nonlinear differential equation (Becker 1998)

$$\frac{d}{d\tau} \left( -\frac{7}{2} \mu^2 + 7\mu + \frac{d\mu}{d\tau} \right) = -\mu^2(7 - 4\mu), \quad (14)$$

where

$$\tau \equiv \tau_{\parallel} \frac{v_c}{c}, \quad \mu \equiv \frac{v}{v_c}. \quad (15)$$

Here  $v_c$  represents the flow velocity at the sonic point, where we set  $x = \tau = 0$  and  $\mathcal{M} = 1$ , with the radiation Mach number  $\mathcal{M}$  defined by

$$\mathcal{M} \equiv \frac{v}{c_s}, \quad c_s^2 \equiv \frac{4P}{3\rho}. \quad (16)$$

The quantity  $c_s$  denotes the speed of sound in the radiation-dominated gas. In the far upstream region, we assume that  $\mathcal{M} \rightarrow \infty$ , which is an excellent approximation in pulsar accretion flows (Basko & Sunyaev 1975, 1976).

Becker (1998) showed that in order for the flow to come to rest at the stellar surface, the parameters  $r_0$ ,  $J$ ,  $\sigma_{\perp}$ , and  $\sigma_{\parallel}$  must satisfy the relation

$$\frac{m_p^2 c^2}{r_0^2 J^2 \sigma_{\perp} \sigma_{\parallel}} = \frac{4}{3}. \quad (17)$$

The corresponding exact solution for the velocity  $v$  as a function of  $\tau$  in the steady state situation of interest here is given by

$$v(\tau) = \frac{7v_c}{8} \left\{ 1 - \tanh \left[ \frac{7}{2} (\tau - \tau_*) \right] \right\}, \quad (18)$$

where

$$\tau_* \equiv \frac{2}{7} \tanh^{-1} \left( \frac{1}{7} \right) \approx 0.041. \quad (19)$$

Note that  $\mu = 1$  at the sonic point ( $\tau = 0$ ) as required. The velocity can also be written as an explicit function of the position  $x$  using (Basko & Sunyaev 1976)

$$v(x) = \frac{7v_c}{4} \left[ 1 - \left( \frac{7}{3} \right)^{-1+x/x_{\text{st}}} \right], \quad (20)$$

where  $x_{\text{st}}$  is the distance between the sonic point and the stellar surface, which can be evaluated using equation (4.16) from Becker (1998) to obtain

$$x_{\text{st}} = \frac{r_0}{2\sqrt{3}} \left( \frac{\sigma_{\perp}}{\sigma_{\parallel}} \right)^{1/2} \ln \left( \frac{7}{3} \right). \quad (21)$$

Note that  $x$  increases in the direction of the flow, which comes to rest at the surface of the star as expected. The height above the stellar surface  $h$  is related to the coordinate  $x$  via

$$h(x) = x_{\text{st}} - x. \quad (22)$$

The incident (upstream) velocity of the infalling material is expected to be close to the free-fall velocity onto the stellar surface,  $v_{\text{ff}}$ , given by

$$v_{\text{ff}} = \left( \frac{2GM_*}{R_*} \right)^{1/2}. \quad (23)$$

Since  $v \rightarrow (7/4)v_c$  in the upstream region according to equation (20), it follows that  $v_c = \frac{4}{7}v_{\text{ff}}$ , and therefore the flow velocity at the sonic point is given by

$$v_c = \frac{4}{7} \left( \frac{2GM_*}{R_*} \right)^{1/2}. \quad (24)$$

With the velocity solution given by equation (20), the corresponding pressure profile can be obtained by combining equations (5) and (6), which yields

$$P(x) = I - Jv(x). \quad (25)$$

The pressure increases to a maximum value at the surface of the star, where  $v \rightarrow 0$ . Based on equations (5) and (16), we can reexpress the Mach number as

$$\mathcal{M} = \left( \frac{3Jv}{4P} \right)^{1/2}. \quad (26)$$

Since the Mach number approaches infinity in the far upstream region and  $v \rightarrow (7/4)v_c$ , it follows that  $P$  must vanish asymptotically and consequently the upstream momentum flux is dominated by the ram pressure of the freely falling matter. We therefore obtain

$$I = Jv_{\text{ff}}. \quad (27)$$

By combining equations (24), (25), and (27), we find that the pressure profile is related to the velocity variation by

$$P(x) = Jv_c \left[ \frac{7}{4} - \frac{v(x)}{v_c} \right]. \quad (28)$$

Using equation (20) to eliminate the velocity  $v(x)$  yields the closed-form result

$$P(x) = \frac{7}{4} Jv_c \left( \frac{7}{3} \right)^{-1+x/x_{\text{st}}}. \quad (29)$$

The pressure vanishes in the upstream limit ( $x \rightarrow -\infty$ ) as expected, and at the surface of the star ( $x = x_{\text{st}}$ ), the pressure achieves the stagnation value

$$P_{\text{st}} \equiv P(x_{\text{st}}) = \frac{7}{4} Jv_c. \quad (30)$$

### 3. RADIATIVE TRANSFER IN THE ACCRETION COLUMN

If the gas is radiation dominated and fully ionized, then the photons interact with the matter primarily via electron scattering, which controls both the spatial transport and the energization of the radiation. In this situation the opacity is dominated by electron scattering, and therefore absorption is negligible, except at the surface of the thermal mound located inside the cylindrical accretion column at  $x = x_0$ . We are interested in obtaining the photon distribution,  $f(x_0, x, \epsilon)$ , measured at position  $x$  and energy  $\epsilon$  resulting from the reprocessing of blackbody radiation emitted from the mound. The normalization of  $f$  is defined so that  $\epsilon^2 f(x_0, x, \epsilon) d\epsilon$  gives the number density of photons in the energy range between  $\epsilon$  and  $\epsilon + d\epsilon$ , and therefore  $f = 8\pi\bar{n}/(c^3 h^3)$ , where  $\bar{n}$  is the occupation number. The self-consistency of the solution obtained for the radiation distribution  $f$  will be confirmed by verifying that the associated pressure distribution agrees with the dynamical result given by equation (29).

#### 3.1. Transport Equation

In the cylindrical geometry employed here, the photon distribution  $f$  satisfies the transport equation (e.g., Blandford & Payne 1981a; Becker 1992; Parker 1965; Becker & Wolff 2005)

$$\begin{aligned} \frac{\partial f}{\partial t} = & -v \frac{\partial f}{\partial x} + \frac{dv}{dx} \frac{\epsilon}{3} \frac{\partial f}{\partial \epsilon} + \frac{\partial}{\partial x} \left( \frac{c}{3n_e \sigma_{\parallel}} \frac{\partial f}{\partial x} \right) \\ & + \frac{S(\epsilon)}{\pi r_0^2} \delta(x - x_0) - \frac{f}{t_{\text{esc}}} - \beta v_0 \delta(x - x_0) f, \end{aligned} \quad (31)$$

where  $\epsilon$  is the photon energy,  $x$  is the spatial coordinate along the column axis, and  $v_0 \equiv v(x_0)$  is the flow velocity at the top of the thermal mound. The terms on the right-hand side of equation (31) represent advection, first-order Fermi energization (“bulk Comptonization”) in the converging flow, spatial diffusion parallel to the column axis, the blackbody source, escape of radiation from the column, and the absorption of radiation at the thermal mound, respectively. We are interested here in the steady state version of equation (31) with  $\partial f/\partial t = 0$ . The photon number and energy densities associated with the distribution  $f$  are given, respectively, by

$$n(x) = \int_0^{\infty} \epsilon^2 f(x_0, x, \epsilon) d\epsilon, \quad U(x) = \int_0^{\infty} \epsilon^3 f(x_0, x, \epsilon) d\epsilon. \quad (32)$$

In the present application, we are primarily interested in exploring the effect of the dynamics itself (i.e., the radiative shock) on the observed X-ray emission. The transport equation (31) therefore does not include additional processes such as thermal Comptonization or cyclotron emission and absorption that are likely to be important in X-ray pulsars. In general, the neglect of thermal Comptonization is reasonable because at the temperatures typical of X-ray pulsars ( $T \sim 10^6 - 10^7$  K), the kinetic energy associated with the bulk flow far surpasses the thermal energy. However, the failure to include the electron recoil associated with thermal Comptonization renders the model unable to reproduce the quasi-exponential cutoffs often observed in X-ray pulsar spectra at high energies. Furthermore, in some sources thermal Comptonization appears to be necessary in order to flatten the spectrum in the energy range  $\epsilon \sim 5 - 20$  keV. We provide further discussion of this issue in § 7.

When integrated over the photon energy spectrum, the first-order Fermi process considered here corresponds to the  $PdV$  work done on the radiation by the compression of the background plasma as it accretes onto the stellar surface. The mean escape time,  $t_{\text{esc}}$ , is given by equation (13), and the source term  $S(\epsilon)$  is defined so that  $\epsilon^2 S(\epsilon) d\epsilon$  represents the number of photons injected into the accretion column per second in the energy range between  $\epsilon$  and  $\epsilon + d\epsilon$  from the blackbody surface at  $x = x_0$ . The absorption term in equation (31) containing the dimensionless constant  $\beta$  must be included due to the blackbody nature of the thermal mound, which acts as both a source and a sink of radiation. In the radiation-dominated situation considered here, essentially all of the pressure is provided by the photons, and therefore the rate of absorption of radiation energy at the top of the mound must equal the energy emission rate when integrated with respect to the photon frequency (see eq. [9]). We use this energy balance argument to compute a self-consistent value for  $\beta$  below.

Next we need to specify the appropriate form for the source term  $S(\epsilon)$  in order to treat the injection of the blackbody radiation from the surface of the thermal mound. The flux per unit energy measured at the surface of an isotropically radiating object is equal to  $\pi$  times the intensity (Rybicki & Lightman 1979). It therefore follows that the amount of energy emitted per second from the upper surface of the thermal mound (with area  $\pi r_0^2$ ) in the energy range between  $\epsilon$  and  $\epsilon + d\epsilon$  is given by

$$\epsilon^3 S(\epsilon) d\epsilon = \pi r_0^2 \pi B_\epsilon(\epsilon) d\epsilon, \quad (33)$$

where

$$B_\epsilon(\epsilon) = \frac{2\epsilon^3}{h^3 c^2} \frac{1}{e^{\epsilon/kT_0} - 1} \quad (34)$$

denotes the blackbody intensity and  $T_0 \equiv T(x_0)$  is the gas temperature at the surface of the mound. Note that the units for  $B_\epsilon$  are  $\text{ergs s}^{-1} \text{sr}^{-1} \text{cm}^{-2} \text{erg}^{-1}$ . Hence, we obtain for the source term

$$S(\epsilon) = \frac{2\pi^2 r_0^2}{h^3 c^2} \frac{1}{e^{\epsilon/kT_0} - 1}, \quad (35)$$

and consequently the total energy injection rate is given by

$$\int_0^\infty \epsilon^3 S(\epsilon) d\epsilon = \pi r_0^2 \sigma T_0^4 \quad (\propto \text{ergs s}^{-1}), \quad (36)$$

where  $\sigma$  is the Stephan-Boltzmann constant.

### 3.2. Energy Balance at the Thermal Mound

In a radiation-dominated X-ray pulsar accretion column, the emission of fresh blackbody radiation energy at the surface of the thermal mound is almost perfectly balanced by the absorption of energy, as expressed by equation (9). Most of the energy appearing in the emergent X-rays is therefore not supplied from the internal energy of the gas, but rather from its bulk kinetic energy, which is transferred directly to the photons via collisions with infalling electrons. We can gain some insight into the energy balance at the thermal mound by rewriting the

steady state version of the transport equation (31) in the flux conservation form (Skilling 1975; Gleeson & Axford 1967)

$$\begin{aligned} \frac{\partial H_\epsilon}{\partial x} = & -\frac{1}{3\epsilon^2} \frac{\partial}{\partial \epsilon} \left( \epsilon^3 v \frac{\partial f}{\partial x} \right) + \frac{S(\epsilon)}{\pi r_0^2} \delta(x - x_0) \\ & - \frac{f}{t_{\text{esc}}} - \beta v_0 \delta(x - x_0) f, \end{aligned} \quad (37)$$

where

$$H_\epsilon \equiv -\frac{c}{3n_e \sigma_\parallel} \frac{\partial f}{\partial x} - \frac{v\epsilon}{3} \frac{\partial f}{\partial \epsilon} \quad (38)$$

represents the ‘‘specific flux’’ (Becker 1992). By operating on equation (37) with  $\int_0^\infty \epsilon^3 d\epsilon$  and utilizing equations (32) and (36), we arrive at the photon energy equation

$$\frac{dQ}{dx} = \frac{v}{3} \frac{dU}{dx} - \frac{U}{t_{\text{esc}}} - \beta v_0 \delta(x - x_0) U + \sigma T_0^4 \delta(x - x_0), \quad (39)$$

where the integrated photon energy flux,  $Q$ , is given by

$$Q \equiv \int_0^\infty \epsilon^3 H_\epsilon d\epsilon = \frac{4}{3} vU - \frac{c}{3n_e \sigma_\parallel} \frac{dU}{dx} \quad (\propto \text{ergs cm}^{-2} \text{s}^{-1}). \quad (40)$$

Equation (39) states that the divergence of the radiation energy flux  $Q$  is equal to the net rate of change of the photon energy density due to the combined influence of compression, escape, absorption, and photon injection. Note that  $Q$  is related to the total energy flux  $E$  via (see eq. [7])

$$E = Q + \frac{1}{2} \rho v^3. \quad (41)$$

Since the absorption and emission of radiation energy must balance at the surface of the mound in the radiation-dominated situation of interest here, we can integrate equation (39) with respect to  $x$  across the mound location to obtain

$$\lim_{\epsilon \rightarrow 0} Q(x_0 + \epsilon) - Q(x_0 - \epsilon) = -\beta v_0 U_0 + \sigma T_0^4 = 0, \quad (42)$$

where  $U_0 \equiv U(x_0)$  denotes the radiation energy density at the mound surface. The fact that the photon energy flux  $Q$  is continuous at  $x = x_0$  therefore requires that the dimensionless absorption constant  $\beta$  in the transport equation (31) be given by

$$\beta = \frac{\sigma T_0^4}{v_0 U_0}. \quad (43)$$

By utilizing this expression for  $\beta$ , we ensure that the results obtained for the radiation spectrum  $f(x_0, x, \epsilon)$  are consistent with the dynamical structure of the accretion column. This is confirmed after the fact by calculating the radiation pressure  $P = U/3$  using equation (32) and comparing the result with the dynamical solution given by equation (29).

## 4. EXACT SOLUTION FOR THE RADIATION SPECTRUM

In our approach to solving equation (31) for the spectrum  $f(x_0, x, \epsilon)$  inside the accretion column, we first obtain the Green’s function,  $f_G(x_0, x, \epsilon_0, \epsilon)$ , which is the radiation distribution at location  $x$  and energy  $\epsilon$  resulting from the injection of  $\dot{N}_0$  photons per second with energy  $\epsilon_0$  from a monochromatic

source at location  $x_0$ . The determination of the Green's function is a useful intermediate step in the process because it provides us with fundamental physical insight into the spectral redistribution process, and it also allows us to calculate the particular solution for the spectrum  $f$  associated with an arbitrary continuum source  $S(\epsilon)$  using the integral convolution (Becker 2003)

$$f(x_0, x, \epsilon) = \int_0^\epsilon \frac{f_G(x_0, x, \epsilon_0, \epsilon)}{N_0} \epsilon_0^2 S(\epsilon_0) d\epsilon_0. \quad (44)$$

Note that the upper bound of integration is set equal to  $\epsilon$  because in our model all of the injected photons gain energy via the first-order Fermi process, and none lose energy. The technical procedure used to solve for the Green's function involves the derivation of eigenfunctions and associated eigenvalues based on the set of spatial boundary conditions for the problem (see, e.g., Blandford & Payne 1981b; Payne & Blandford 1981; Schneider & Kirk 1987; Colpi 1988).

The steady state transport equation governing the Green's function is (cf. eq. [31])

$$\begin{aligned} v \frac{\partial f_G}{\partial x} &= \frac{dv}{dx} \frac{\epsilon}{3} \frac{\partial f_G}{\partial \epsilon} + \frac{\partial}{\partial x} \left( \frac{c}{3n_e \sigma_{\parallel}} \frac{\partial f_G}{\partial x} \right) \\ &+ \frac{\dot{N}_0 \delta(\epsilon - \epsilon_0) \delta(x - x_0)}{\pi r_0^2 \epsilon_0^2} - \frac{f_G}{t_{\text{esc}}} - \beta v_0 \delta(x - x_0) f_G, \end{aligned} \quad (45)$$

and the associated radiation number and energy densities are given by (cf. eq. [32])

$$\begin{aligned} n_G(x) &\equiv \int_0^\infty \epsilon^2 f_G(x_0, x, \epsilon_0, \epsilon) d\epsilon, \\ U_G(x) &\equiv \int_0^\infty \epsilon^3 f_G(x_0, x, \epsilon_0, \epsilon) d\epsilon. \end{aligned} \quad (46)$$

Further simplification of the mathematical derivation is possible if we work in terms of the new spatial variable  $y$ , defined by

$$y(x) \equiv \left( \frac{7}{3} \right)^{-1+x/x_{\text{st}}}, \quad (47)$$

where  $x_{\text{st}}$  is given by equation (21). Note that  $y \rightarrow 0$  in the far upstream region ( $x \rightarrow -\infty$ ) and  $y \rightarrow 1$  at the surface of the star ( $x \rightarrow x_{\text{st}}$ ).

Based on equations (20) and (47), we find that the variation of the velocity  $v$  as a function of the new variable  $y$  is given by the simple expression

$$v(y) = \frac{7v_c}{4}(1-y). \quad (48)$$

Likewise, we can also combine equations (29) and (47) to show that the exact dynamical solution for the radiation pressure profile as a function of  $y$  is given by

$$P(y) = \frac{7}{4} J v_c y. \quad (49)$$

Note that in the limit  $y \rightarrow 1$ , the pressure approaches the stagnation value  $P_{\text{st}} \equiv (7/4) J v_c$  in agreement with equation (30). Equations (29) and (49) prove useful when we seek to confirm

the validity of the results obtained for the photon distribution  $f(x_0, x, \epsilon)$  in § 5.

Utilizing equations (5), (13), (17), and (48) along with the differential relation

$$\frac{dx}{dy} = \frac{r_0}{2\sqrt{3}} \left( \frac{\sigma_{\perp}}{\sigma_{\parallel}} \right)^{1/2} y^{-1}, \quad (50)$$

we find that equation (45) can be transformed from  $x$  to  $y$  to obtain

$$\begin{aligned} y(1-y) \frac{\partial^2 f_G}{\partial y^2} + \left( \frac{1-5y}{4} \right) \frac{\partial f_G}{\partial y} - \frac{\epsilon}{4} \frac{\partial f_G}{\partial \epsilon} + \left( \frac{y-1}{4y} \right) f_G \\ = \frac{3\beta v_0 \delta(y-y_0) f_G}{7v_c} - \frac{3\dot{N}_0 \delta(\epsilon - \epsilon_0) \delta(y-y_0)}{7\pi r_0^2 \epsilon_0^2 v_c}, \end{aligned} \quad (51)$$

where we have made the definition

$$y_0 \equiv y(x_0) = \left( \frac{7}{3} \right)^{-1+x_0/x_{\text{st}}}, \quad (52)$$

so that  $y_0$  denotes the value of  $y$  at the top of the thermal mound (see eq. [47]). According to equation (48), the flow velocity at the top of the mound,  $v_0$ , is related to  $y_0$  via

$$\frac{v_0}{v_c} = \frac{7}{4}(1-y_0). \quad (53)$$

Note that we can now write the Green's function as either  $f_G(x_0, x, \epsilon_0, \epsilon)$  or  $f_G(y_0, y, \epsilon_0, \epsilon)$  since  $(x, x_0)$  and  $(y, y_0)$  are interchangeable via equations (47) and (52).

#### 4.1. Separation Solutions

When  $\epsilon > \epsilon_0$ , equation (51) is separable in energy and space using the functions

$$f_{\lambda}(\epsilon, y) = \epsilon^{-\lambda} g(\lambda, y), \quad (54)$$

where  $\lambda$  is the separation constant and the spatial function  $g$  satisfies the differential equation

$$\begin{aligned} y(1-y) \frac{d^2 g}{dy^2} + \left( \frac{1-5y}{4} \right) \frac{dg}{dy} + \left( \frac{\lambda y + y - 1}{4y} \right) g \\ = \frac{3\beta v_0 \delta(y-y_0)}{7v_c} g. \end{aligned} \quad (55)$$

In order to avoid an infinite spatial diffusion flux at  $y = y_0$ , the function  $g$  must be continuous there, and consequently we obtain the condition

$$\lim_{\epsilon \rightarrow 0} g(\lambda, y_0 + \epsilon) - g(\lambda, y_0 - \epsilon) = 0. \quad (56)$$

We can also derive a jump condition for the derivative  $dg/dy$  at the top of the mound by integrating equation (55) with respect to  $y$  in a very small region around  $y = y_0$ . The result obtained is

$$\lim_{\epsilon \rightarrow 0} \frac{dg}{dy} \Big|_{y=y_0+\epsilon} - \frac{dg}{dy} \Big|_{y=y_0-\epsilon} = \frac{3\beta}{4y_0} g(\lambda, y_0), \quad (57)$$

where we have also used equation (53). The spatial eigenfunctions for our problem are denoted by

$$g_n(y) \equiv g(\lambda_n, y), \quad (58)$$

where  $\lambda_n$  represents the  $n$ th eigenvalue. These functions satisfy the continuity and derivative jump conditions given by equations (56) and (57), respectively, as well as the boundary conditions discussed below.

The homogeneous version of equation (55) for  $g$  obtained when  $y \neq y_0$  has fundamental solutions given by

$$\varphi_1(\lambda, y) \equiv yF(a, b; c; y), \quad (59)$$

$$\varphi_1^*(\lambda, y) \equiv y^{-1/4}F(a - 5/4, b - 5/4; 2 - c; y), \quad (60)$$

where  $F(a, b; c; z)$  denotes the hypergeometric function (Abramowitz & Stegun 1970) and the parameters  $a$ ,  $b$ , and  $c$  are defined by

$$a \equiv \frac{9 - \sqrt{17 + 16\lambda}}{8}, \quad b \equiv \frac{9 + \sqrt{17 + 16\lambda}}{8}, \quad c \equiv \frac{9}{4}. \quad (61)$$

The “seed” photons injected into the flow from the thermal mound located near the base of the column are unable to diffuse very far up into the accreting gas due to the extremely high speed of the inflow. Most of the photons therefore escape through the walls of the column within a few scattering lengths of the mound, forming a “fan”-type beam pattern, as expected for accretion-powered X-ray pulsars (e.g., Harding 1994, 2003). Based on this physical picture, we conclude that the eigenfunction  $g_n$  must *vanish* in the upstream limit,  $y \rightarrow 0$ . Conversely, in the downstream limit,  $y \rightarrow 1$ , the gas settles onto the surface of the star and the radiation pressure achieves the stagnation value given by equation (30). Since this is a finite pressure, we conclude that  $g_n$  must approach a constant as  $y \rightarrow 1$ .

Analysis of the asymptotic behaviors of the hypergeometric functions  $\varphi_1$  and  $\varphi_1^*$  shows that the first function vanishes and the second diverges as  $y \rightarrow 0$ . Hence, in the region upstream from the thermal mound ( $y \leq y_0$ ), the eigenfunction  $g_n$  must be given by  $\varphi_1$ . However, in the downstream region ( $y \geq y_0$ ), the situation is more complicated because the two functions  $\varphi_1$  and  $\varphi_1^*$  each diverge logarithmically as  $y \rightarrow 1$ . We must therefore utilize a suitable linear combination of these functions in order to obtain a convergent solution in the downstream region. Consequently, we define the new function (see Appendix A for details)

$$\varphi_2(\lambda, y) \equiv \frac{\Gamma(b)}{\Gamma(c)\Gamma(1-b)}\varphi_1(\lambda, y) - \frac{\Gamma(1-a)}{\Gamma(2-c)\Gamma(a)}\varphi_1^*(\lambda, y), \quad (62)$$

which remains finite in the limit  $y \rightarrow 1$  as required.

#### 4.2. Eigenfunctions and Eigenvalues

By utilizing the various relations derived above, we find that the global solution for the spatial eigenfunction  $g_n(y)$  (eq. [58]) can now be written as

$$g_n(y) = \begin{cases} \varphi_1(\lambda_n, y), & y \leq y_0, \\ B_n \varphi_2(\lambda_n, y), & y \geq y_0, \end{cases} \quad (63)$$

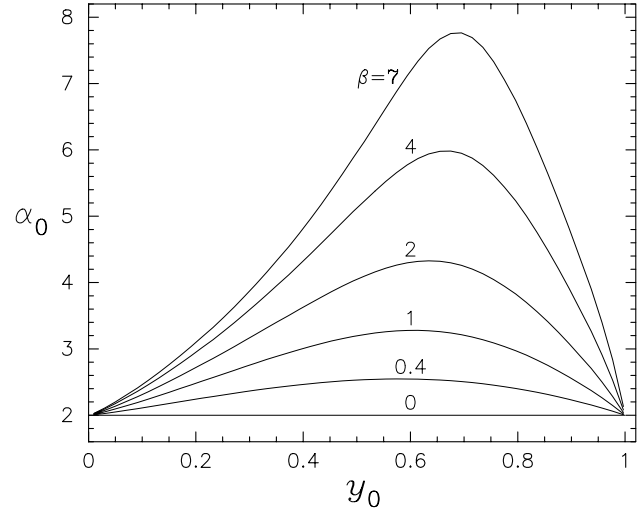


FIG. 2.—High-energy power-law photon spectral index  $\alpha_0$  plotted as a function of the source location  $y_0$  for the indicated values of the absorption parameter  $\beta$ . Note the steepening of the radiation spectrum that occurs when  $\beta$  is increased for a fixed value of  $y_0$ , which reflects the decreasing residence time for the photons in the plasma due to the enhanced absorption.

where the constant  $B_n$  is determined using the continuity condition (eq. [56]), which yields

$$B_n = \frac{\varphi_1(\lambda_n, y_0)}{\varphi_2(\lambda_n, y_0)}. \quad (64)$$

We can combine equations (57), (63), and (64) to show that the eigenvalue equation for  $\lambda$  is given by

$$\varphi_1 \frac{\partial \varphi_2}{\partial y} - \varphi_2 \frac{\partial \varphi_1}{\partial y} - \frac{3\beta \varphi_1 \varphi_2}{4y} \Big|_{y=y_0} = 0. \quad (65)$$

The left-hand side of this expression can be evaluated using the exact solution for the Wronskian (see Appendix B),

$$W(\lambda, y) \equiv \varphi_1 \frac{\partial \varphi_2}{\partial y} - \varphi_2 \frac{\partial \varphi_1}{\partial y} = \frac{5}{4} \frac{\Gamma(1-a)}{\Gamma(a)\Gamma(2-c)} \frac{y^{-1/4}}{1-y}, \quad (66)$$

which is applicable for arbitrary values of  $\lambda$  and  $y$ . Equations (65) and (66) can be combined to obtain the alternative form for the eigenvalue equation,

$$\frac{5}{3} \frac{\Gamma(1-a)}{\Gamma(a)\Gamma(2-c)} \frac{y_0^{3/4}}{1-y_0} = \beta \varphi_1(\lambda, y_0) \varphi_2(\lambda, y_0), \quad (67)$$

where  $a$ ,  $b$ , and  $c$  are functions of  $\lambda$  given by equation (61). The roots of this expression are the eigenvalues  $\lambda = \lambda_n$ , and the associated eigenfunctions are evaluated using equation (63). In the limit  $\beta \rightarrow 0$ , which corresponds to no absorption, equation (67) simplifies considerably and one finds that the eigenvalues are given by the explicit relation  $\lambda_n = 4n^2 + 9n + 4$ .

The first eigenvalue,  $\lambda_0$ , is especially important because it determines the slope of the high-energy spectrum emerging from the accretion column according to equation (54). The spectral index of the emitted photon count rate distribution,  $\alpha_0$ , is related to  $\lambda_0$  via  $\alpha_0 = \lambda_0 - 2$ . In Figure 2 we plot the photon index  $\alpha_0$  as a function of the dimensionless parameters  $\beta$  and  $y_0$ . Note that  $\alpha_0$  is a double-valued function of  $y_0$  for fixed  $\beta$ , which is a consequence of the imposed velocity profile (eq. [48]).

Physically, this behavior reflects the fact that it is always possible to achieve a desired amount of compression (first-order Fermi energization) by placing the source in a specific location in either the upstream or downstream region of the flow. We also observe that if we increase the absorption parameter  $\beta$  while holding  $y_0$  fixed, then  $\alpha_0$  increases monotonically, and therefore the high-energy spectrum becomes progressively steeper. This behavior is expected because as the absorption parameter is increased, the injected photons spend less time on average being energized by collisions with electrons before either escaping from the column or being absorbed at the source location. The reduction in the amount of energization naturally leads to a steepening of the radiation spectrum. When  $\beta = 0$ , no absorption occurs, and the index  $\alpha_0$  achieves its minimum (limiting) value of 2. This limit is unphysical, however, since it yields a divergent result for the total photon energy density  $U_G$  according to equation (46).

#### 4.3. Eigenfunction Expansion

We demonstrate in Appendix C that the eigenfunctions  $g_n(y)$  form an orthogonal set, as expected since this is a standard Sturm-Liouville problem. Once the eigenvalues and eigenfunctions are determined, the solution for the Green's function can therefore be expressed as the infinite series

$$f_G(y_0, y, \epsilon_0, \epsilon) = \epsilon^{-3} \sum_{n=0}^{\infty} C_n \left( \frac{\epsilon}{\epsilon_0} \right)^{3-\lambda_n} g_n(y), \quad (68)$$

where the expansion coefficients  $C_n$  are computed by employing the orthogonality of the eigenfunctions along with the condition

$$f_G(y_0, y, \epsilon_0, \epsilon) \Big|_{\epsilon=\epsilon_0} = \frac{12\dot{N}_0}{7\pi r_0^2 \epsilon_0^3 v_c} \delta(y - y_0), \quad (69)$$

which is obtained by integrating the transport equation (51) with respect to  $\epsilon$  in a very small range surrounding the injection energy  $\epsilon_0$ . The result obtained for the  $n$ th expansion coefficient is

$$C_n = \frac{12\dot{N}_0 y_0^{-3/4} g_n(y_0)}{7\pi r_0^2 v_c I_n}, \quad (70)$$

where the quadratic normalization integrals  $I_n$  are defined by

$$I_n \equiv \int_0^1 y^{-3/4} g_n^2(y) dy. \quad (71)$$

In Appendix D we show that the normalization integrals can be evaluated using the closed-form expression

$$I_n = K(\lambda_n, y_0), \quad (72)$$

where

$$K(\lambda, y) \equiv 3\beta y^{-3/4} (1-y) \varphi_1^2(\lambda, y) \times \left[ \frac{\Psi(a) + \Psi(1-a)}{(17+16\lambda)^{1/2}} - \frac{\partial \ln \varphi_1}{\partial \lambda} - \frac{\partial \ln \varphi_2}{\partial \lambda} \right], \quad (73)$$

with

$$\Psi(z) \equiv \frac{1}{\Gamma(z)} \frac{d\Gamma(z)}{dz}. \quad (74)$$

This provides an extremely efficient alternative to numerical integration for the computation of  $I_n$ . The eigenfunction expansion converges rapidly, and therefore we are able to obtain an accuracy of at least five significant figures in our calculations of  $f_G$  by terminating the series in equation (68) after the first 20 terms.

#### 4.4. Green's Function for the Escaping Photon Spectrum

Equation (68) represents the exact solution for the Green's function describing the radiation spectrum inside a pulsar accretion column resulting from the injection of  $\dot{N}_0$  seed photons per unit time from a monochromatic source located at  $y = y_0$  (or, equivalently, at  $x = x_0$ ). In the escape probability approach employed here, the associated Green's function for the *photon number spectrum* emitted through the walls of the cylindrical column is defined by

$$\dot{N}_\epsilon^G(x_0, x, \epsilon_0, \epsilon) \equiv \frac{\pi r_0^2 \epsilon^2}{t_{\text{esc}}} f_G(x_0, x, \epsilon_0, \epsilon), \quad (75)$$

so that  $\dot{N}_\epsilon^G dx d\epsilon$  represents the number of photons escaping from the column per unit time between positions  $x$  and  $x + dx$  with energy between  $\epsilon$  and  $\epsilon + d\epsilon$ . We remind the reader that the quantities  $(x, x_0)$  and  $(y, y_0)$  are interchangeable via equations (47) and (52), and therefore we are free to work in terms of the more convenient parameters  $(y, y_0)$  without loss of generality. By substituting for  $t_{\text{esc}}$  using equation (13), we can obtain the alternative expression

$$\dot{N}_\epsilon^G(y_0, y, \epsilon_0, \epsilon) = \frac{\pi m_p c v(y) \epsilon^2}{J \sigma_\perp} f_G(y_0, y, \epsilon_0, \epsilon). \quad (76)$$

Eliminating  $J$  using equation (17) and substituting for  $v$  and  $f_G$  using equations (48) and (68), respectively, yields the equivalent result

$$\dot{N}_\epsilon^G(y_0, y, \epsilon_0, \epsilon) = (1-y) \epsilon^{-1} \sum_{n=0}^{\infty} D_n \left( \frac{\epsilon}{\epsilon_0} \right)^{3-\lambda_n} g_n(y), \quad (77)$$

where the expansion coefficients  $D_n$  are defined by

$$D_n \equiv \frac{2\sqrt{3}\dot{N}_0 g_n(y_0)}{r_0 y_0^{3/4} I_n} \left( \frac{\sigma_\parallel}{\sigma_\perp} \right)^{1/2}. \quad (78)$$

The Green's function  $\dot{N}_\epsilon^G$  describes the photon distribution escaping from the accretion column as a function of energy  $\epsilon$  and location  $y$  for the case of monoenergetic photon injection. Analysis of  $\dot{N}_\epsilon^G$  therefore reveals some interesting details about the energization of the photons as they are transported through the column via diffusion and advection and ultimately escape through the column walls. We plot  $\dot{N}_\epsilon^G$  as a function of the energy ratio  $\epsilon/\epsilon_0$  and the location  $y$  in Figure 3 for the parameter values  $\beta = 0.4$  and  $y_0 = 0.9$ . In this case the first eigenvalue is given by  $\lambda_0 = 4.231$ , and the corresponding photon index is  $\alpha_0 = 2.231$  (see Fig. 2). The selected value of  $y_0$  corresponds to a source located near the bottom of the accretion column, just above the stellar surface. At the source location,  $y = y_0 = 0.9$ , the energy

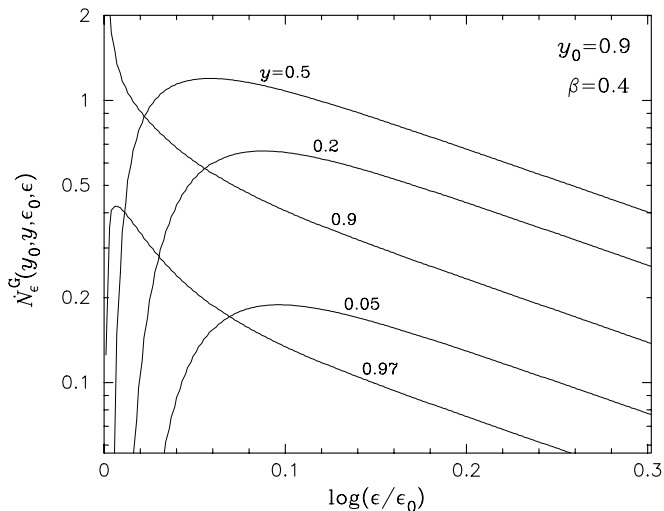


FIG. 3.—Green's function  $\dot{N}_\epsilon^G(y_0, y, \epsilon_0, \epsilon)$  describing the photon distribution escaping from the accretion column per unit time (eq. [77]) plotted in units of  $\dot{N}_0(\sigma_\parallel/\sigma_\perp)^{1/2}(r_0\epsilon_0)^{-1}$  as a function of the photon energy ratio  $\epsilon/\epsilon_0$  for the indicated values of the spatial variable  $y$ . In this example we have set the absorption constant  $\beta = 0.4$  and the source location  $y_0 = 0.9$ , so that the monoenergetic source is located near the base of the accretion column.

spectrum extends down to the injection energy,  $\epsilon_0$ . However, at all other radii the spectrum displays a steep turnover above  $\epsilon_0$  because all of the photons at these locations have experienced Fermi energization due to collisions with the infalling electrons. The photons with energy  $\epsilon = \epsilon_0$  at the source location have been injected so recently that they have not yet experienced significant energization. Note that for small values of  $y$ , the escaping spectrum is greatly attenuated due to the inability of the photons to diffuse upstream through the rapidly infalling plasma. The escaping spectrum is also attenuated in the far downstream region ( $y \sim 1$ ) due to the very high opacity of the flow, which inhibits the diffusion of photons through the walls. The latter effect stems from the divergence of the electron density near the stellar surface. The energy of maximum brightness, corresponding to the peak in  $\dot{N}_\epsilon^G$ , achieves its maximum value as  $y \rightarrow 0$  because the photons that manage to diffuse far upstream from the source are the ones that have resided in the flow the longest and therefore experienced the most energy amplification.

We plot  $\dot{N}_\epsilon^G$  as a function of energy and location in Figure 4 for the parameters  $\beta = 4$  and  $y_0 = 0.4$ , in which case we obtain for the first eigenvalue and the photon index  $\lambda_0 = 6.325$  and  $\alpha_0 = 4.325$ , respectively. In this scenario the source is located in the upstream region and the absorption is stronger than that in Figure 3. Due to the increased absorption resulting from the larger value of  $\beta$ , the photons spend less time on average in the flow being energized by collisions with the electrons before they escape through the column walls or are “recycled” by absorption. This causes a steepening of the spectrum at high energies, as evidenced by the increase in the photon index  $\alpha_0$ . In this situation the energy of maximum brightness (where  $\dot{N}_\epsilon^G$  displays a peak) achieves its greatest value in the downstream region. This is the reverse of the behavior displayed in Figure 3 because in the present example the source is located in the upstream region and therefore the photons that diffuse farther upstream toward  $y = 0$  do not experience as much compression as those that are advected downstream. The escaping photon distribution in the far upstream and downstream regions is strongly attenuated due to the same processes operative in

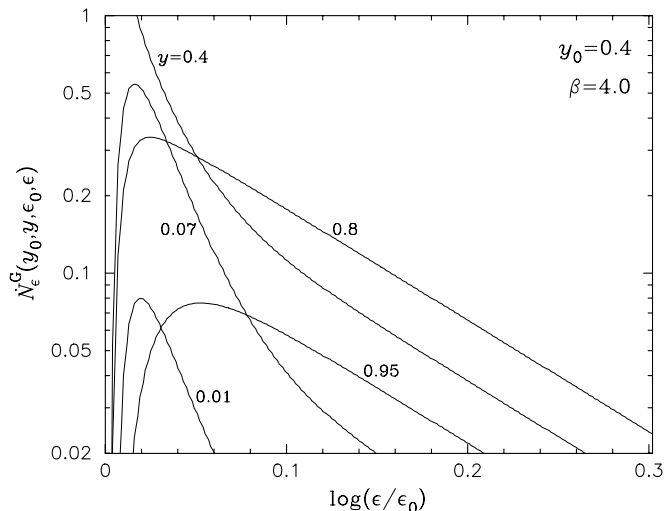


FIG. 4.—Same as Fig. 3, except  $\beta = 4.0$  and  $y_0 = 0.4$ . In this case the source is located in the upstream region, and the absorption at the source location is stronger than in Fig. 3. The latter effect causes a significant steepening of the spectrum at high energies, as explained in the text.

Figure 3, and therefore most of the escaping radiation is emitted from the accretion column around the source location.

The analytical results for the Green's function obtained in this section provide the basis for the consideration of any source distribution since the fundamental differential equation (31) is linear. This is further discussed in § 5, where we use equations (35) and (44) to convolve the Green's function with the blackbody spectrum produced by the thermal mound.

#### 4.5. Column-integrated Green's Function

By integrating over the vertical structure of the accretion column, we can compute the total emitted radiation distribution, which corresponds to the phase-averaged spectrum of the X-ray pulsar. In the cylindrical geometry employed here, the formal integration domain is the region  $-\infty < x < x_{st}$ , where  $x_{st}$  is the distance between the sonic point and the stellar surface (see eq. [21]). For the case of a monochromatic source, we define the *column-integrated Green's function* by writing

$$\Phi_\epsilon^G(x_0, \epsilon_0, \epsilon) \equiv \int_{-\infty}^{x_{st}} \dot{N}_\epsilon^G(x_0, x, \epsilon_0, \epsilon) dx, \quad (79)$$

where  $\Phi_\epsilon^G d\epsilon$  represents the number of photons escaping from the column per unit time with energy between  $\epsilon$  and  $\epsilon + d\epsilon$ . Using equation (50), the variable of integration can be transformed from  $x$  to  $y$  to obtain the alternative form

$$\Phi_\epsilon^G(y_0, \epsilon_0, \epsilon) = \frac{r_0}{2\sqrt{3}} \left( \frac{\sigma_\perp}{\sigma_\parallel} \right)^{1/2} \int_0^1 \dot{N}_\epsilon^G(y_0, y, \epsilon_0, \epsilon) \frac{dy}{y}, \quad (80)$$

where  $y_0$  is related to  $x_0$  via equation (52). Despite the appearance of the factor  $y^{-1}$  inside the integral in equation (80), the contribution from small values of  $y$  is actually negligible because the spectrum declines exponentially in the upstream region due to advection. Furthermore, the escaping spectrum is also strongly attenuated in the downstream region due to the divergence of the electron density. Hence, most of the radiation is emitted from the column around  $y \sim 0.5$ , as indicated in Figures 3 and 4.

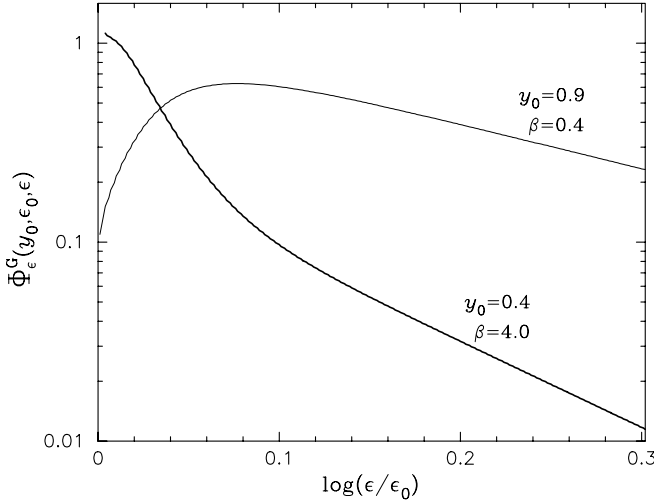


FIG. 5.—Column-integrated Green's function  $\Phi_\epsilon^G(y_0, \epsilon_0, \epsilon)$  describing the photon spectrum escaping through the walls of the accretion column (eq. [81]) plotted in units of  $\dot{N}_0/\epsilon_0$  as a function of the photon energy ratio  $\epsilon/\epsilon_0$ . The parameter values used are  $y_0 = 0.9$ ,  $\beta = 0.4$  (thin line) and  $y_0 = 0.4$ ,  $\beta = 4.0$  (thick line), which correspond to the spectra plotted in Figs. 3 and 4, respectively.

By combining equations (77), (78), and (80), we can reexpress the column-integrated Green's function as

$$\Phi_\epsilon^G(y_0, \epsilon_0, \epsilon) = \frac{\dot{N}_0}{\epsilon y_0^{3/4}} \sum_{n=0}^{\infty} \frac{g_n(y_0)}{I_n} \left(\frac{\epsilon}{\epsilon_0}\right)^{3-\lambda_n} X_n, \quad (81)$$

where the quadratic normalization integrals  $I_n$  are evaluated using equation (72) and we have made the definition

$$X_n \equiv \int_0^1 g_n(y)(1-y)y^{-1} dy. \quad (82)$$

In Appendix E we demonstrate that the integral in the expression for  $X_n$  can be carried out analytically to obtain

$$\begin{aligned} X_n = & \frac{\Gamma(1-a)(1-y_0)^2}{\Gamma(a)\varphi_2(\lambda_n, y_0)} \left\{ \frac{y_0^{2-c}\varphi_1(\lambda_n, y_0)}{\Gamma(3-c)} \right. \\ & \times \left[ F(2-a, 2-b; 3-c; y_0) \right. \\ & \left. + \frac{y_0}{3-c} F(3-a, 3-b; 4-c; y_0) \right] \\ & + \frac{\varphi_1^*(\lambda_n, y_0)}{(a-1)(b-1)\Gamma(1-c)} \left[ F(a, b; c-1; y_0) \right. \\ & \left. + \frac{(c-2)}{(a-2)(b-2)} F(a, b; c-2; y_0) \right] \left. \right\} \\ & + \frac{(1-c)}{(a-1)(b-1)} \left[ 1 + \frac{(c-2)}{(a-2)(b-2)} \right], \quad (83) \end{aligned}$$

where  $\varphi_1(\lambda_n, y_0)$ ,  $\varphi_1^*(\lambda_n, y_0)$ , and  $\varphi_2(\lambda_n, y_0)$  are given by equations (59), (60), and (62), respectively, and the constants  $a$ ,  $b$ , and  $c$  are computed in terms of  $\lambda_n$  using equation (61).

In Figure 5 we plot the dependence of the column-integrated Green's function  $\Phi_\epsilon^G$  on the radiation energy  $\epsilon$  using the same parameters employed in Figures 3 and 4. Note that when  $\beta = 0.4$  and  $y_0 = 0.9$ , which corresponds to the thin line in Figure 5, the column-integrated spectrum displays a peak at  $\epsilon/\epsilon_0 \sim 1.5$ . The peak forms because the source is located close

to the bottom of the accretion column, whereas most of the photons escape from higher altitudes around  $y \sim 0.5$  (see Fig. 3). The escaping radiation has therefore experienced significant compression in the flow and consequently the photon energies are generally boosted above the injection energy  $\epsilon_0$ . On the other hand, when  $\beta = 4$  and  $y_0 = 0.4$ , which corresponds to the thick line in Figure 5, the absorption is so strong that the spectrum is quite steep and therefore the peak is suppressed. Consequently, the column-integrated spectrum achieves its maximum value at the injection energy in this case.

#### 4.6. Reprocessed Blackbody Radiation

The closed-form solutions for the Green's function  $\dot{N}_\epsilon^G$  (eq. [77]) and for the column-integrated Green's function  $\Phi_\epsilon^G$  (eq. [81]) provide a very efficient means for computing the X-ray spectrum escaping through the walls of the accretion column due to the injection of monochromatic seed photons. However, in our physical application to X-ray pulsars, we are primarily interested in computing the emitted spectrum resulting from the reprocessing of *blackbody radiation* injected into the accretion column from the thermal mound. In the escape probability approach utilized here, the photon distribution emitted through the walls of the cylindrical column at position  $x$ , denoted by  $\dot{N}_\epsilon(x_0, x, \epsilon)$ , is computed using

$$\dot{N}_\epsilon(x_0, x, \epsilon) \equiv \frac{\pi r_0^2 \epsilon^2}{t_{\text{esc}}} f(x_0, x, \epsilon), \quad (84)$$

where the particular solution  $f(x_0, x, \epsilon)$  is evaluated using equation (44) and  $\dot{N}_\epsilon dx d\epsilon$  represents the number of photons escaping from the column per unit time between positions  $x$  and  $x + dx$  with energy between  $\epsilon$  and  $\epsilon + d\epsilon$ . By combining equations (44) and (84), we find that the escaping photon spectrum can be expressed as

$$\dot{N}_\epsilon(x_0, x, \epsilon) = \frac{\pi r_0^2 \epsilon^2}{t_{\text{esc}}} \int_0^\epsilon \frac{f_G(x_0, x, \epsilon_0, \epsilon)}{\dot{N}_0} \epsilon_0^2 S(\epsilon_0) d\epsilon_0, \quad (85)$$

where the blackbody source function  $S(\epsilon_0)$  is evaluated using equation (35). The spatial variables  $(x, x_0)$  and  $(y, y_0)$  are interchangeable by virtue of equations (47) and (52), and therefore we can use equations (75) and (85) to write

$$\dot{N}_\epsilon(y_0, y, \epsilon) = \int_0^\epsilon \frac{\dot{N}_\epsilon^G(y_0, y, \epsilon_0, \epsilon)}{\dot{N}_0} \epsilon_0^2 S(\epsilon_0) d\epsilon_0, \quad (86)$$

where  $\dot{N}_\epsilon^G(y_0, y, \epsilon_0, \epsilon)$  is computed using equation (77).

By analogy with equation (79) for the Green's function, we define the particular solution for the *column-integrated* photon spectrum escaping from the plasma due to the blackbody source,  $\Phi_\epsilon(x_0, \epsilon)$ , by writing

$$\Phi_\epsilon(x_0, \epsilon) \equiv \int_{-\infty}^{x_{\text{st}}} \dot{N}_\epsilon(x_0, x, \epsilon) dx, \quad (87)$$

so that  $\Phi_\epsilon d\epsilon$  gives the number of photons escaping from the column per unit time with energy between  $\epsilon$  and  $\epsilon + d\epsilon$ . The variable of integration can be transformed from  $x$  to  $y$  using equation (50), which yields

$$\Phi_\epsilon(y_0, \epsilon) = \frac{r_0}{2\sqrt{3}} \left(\frac{\sigma_\perp}{\sigma_\parallel}\right)^{1/2} \int_0^1 \dot{N}_\epsilon(y_0, y, \epsilon) \frac{dy}{y}, \quad (88)$$

where  $y_0$  is related to  $x_0$  by equation (52). By substituting for  $\dot{N}_\epsilon$  using equation (86) and employing equation (80), we can obtain the alternative form

$$\Phi_\epsilon(y_0, \epsilon) = \int_0^\epsilon \frac{\Phi_\epsilon^G(y_0, \epsilon_0, \epsilon)}{\dot{N}_0} \epsilon_0^2 S(\epsilon_0) d\epsilon_0. \quad (89)$$

The column-integrated Green's function  $\Phi_\epsilon^G(y_0, \epsilon_0, \epsilon)$  is evaluated using equation (81). In § 5 we utilize equations (86) and (89) to compute the photon spectrum emitted from the accretion column using parameters corresponding to specific X-ray pulsars.

## 5. ASTROPHYSICAL APPLICATIONS

For given values of the stellar mass  $M_*$  and the stellar radius  $R_*$ , our model has three free parameters, namely, the column radius  $r_0$ , the temperature at the top of the thermal mound  $T_0$ , and the accretion rate  $\dot{M}$ . In this section we investigate the relationship between these quantities and the dimensionless parameters  $y_0$  and  $\beta$  appearing in the theory. Although it is not our intention in this paper to develop complete models for X-ray pulsar spectra, it is nonetheless interesting to compare the simplified model developed here with actual data for a few sources. Hence, in this section we also compute the spectrum emerging from the accretion column for parameters corresponding to two specific X-ray pulsars.

### 5.1. Location of the Thermal Mound

In order to understand how the theory developed here can be related to observables such as the temperature and the luminosity, we first need to determine how the position of the thermal mound,  $x_0$  (or, equivalently,  $y_0$ ), depends on the values of  $r_0$ ,  $T_0$ , and  $\dot{M}$ . The blackbody surface of the mound represents the photosphere for photon creation and destruction in this problem, and therefore the opacity is dominated by free-free absorption inside the mound. For a given value of the temperature  $T_0$ , the density at the top of the mound,  $\rho_0$ , can be calculated by setting the free-free optical thickness of the column equal to unity, so that

$$\tau_0^{\text{ff}} \equiv r_0 \alpha_{\text{R}}^{\text{ff}}(r_0) = 1, \quad (90)$$

where the Rosseland mean of the free-free absorption coefficient is evaluated in cgs units using (Rybicki & Lightman 1979)

$$\alpha_{\text{R}}^{\text{ff}}(r_0) = 6.10 \times 10^{22} T_0^{-7/2} \rho_0^2, \quad (91)$$

for pure, fully ionized hydrogen with the Gaunt factor set equal to unity. The density at the top of the thermal mound is therefore given by

$$\rho_0 = 4.05 \times 10^{-12} T_0^{7/4} r_0^{-1/2}. \quad (92)$$

The velocity at the top of the mound,  $v_0$ , is related to  $\rho_0$  via the continuity equation  $\dot{M} = \pi r_0^2 v_0 \rho_0$ , so that

$$v_0 = 7.86 \times 10^{10} \dot{M} r_0^{-3/2} T_0^{-7/4}. \quad (93)$$

By combining this result with equations (24) and (53), we find that the value of  $y_0$  is given by

$$y_0 = 1 - 2.15 \times 10^{14} R_*^{1/2} M_*^{-1/2} \dot{M} r_0^{-3/2} T_0^{-7/4}, \quad (94)$$

or, equivalently,

$$y_0 = 1 - 8.57 \times 10^{-4} \left( \frac{R_*}{10 \text{ km}} \right)^{1/2} \left( \frac{M_*}{M_\odot} \right)^{-1/2} \times \left( \frac{\dot{M}}{10^{16} \text{ g s}^{-1}} \right) \left( \frac{r_0}{1 \text{ km}} \right)^{-3/2} \left( \frac{T_0}{10^7 \text{ K}} \right)^{-7/4}. \quad (95)$$

The values obtained for  $y_0$  are extremely close to unity, indicating that the top of the thermal mound is just above the stellar surface. Once  $y_0$  is computed, we can determine  $x_0$  by using equation (52) to write

$$\frac{x_0}{x_{\text{st}}} = 1 + \frac{\ln y_0}{\ln(7/3)}, \quad (96)$$

where  $x_{\text{st}}$  is the distance between the sonic point and the stellar surface given by equation (21). The height of the thermal mound above the stellar surface is then given by (see eq. [22])

$$h_0 \equiv h(x_0) = \frac{\ln(1/y_0)}{\ln(7/3)} x_{\text{st}}, \quad (97)$$

or, equivalently,

$$h_0 = \frac{r_0}{2\sqrt{3}} \left( \frac{\sigma_\perp}{\sigma_\parallel} \right)^{1/2} \ln \left( \frac{1}{y_0} \right), \quad (98)$$

where we have substituted for  $x_{\text{st}}$  using equation (21). Specific numerical examples are given in § 5.4. For typical X-ray pulsar parameters, we find that the mound is situated very close to the surface of the star, as expected.

### 5.2. Computation of the Eigenvalues

In order to compute the eigenvalues  $\lambda_n$  using equation (67), we must also evaluate the dimensionless absorption parameter  $\beta$  appearing in the transport equation (31). Based on energy conservation considerations in the radiation-dominated plasma, we have shown in § 3.2 that the photon energy flux  $Q$  must be continuous across the location of the thermal mound. This leads to equation (43), which can be rewritten as

$$\beta = \frac{\sigma T_0^4}{3v_0 P_0}, \quad (99)$$

where  $P_0 = U_0/3$  is the radiation pressure at the top of the thermal mound. According to equation (49),  $P_0 = (7/4) J v_c y_0$ , and therefore

$$\beta = \frac{4\sigma T_0^4}{21 J v_c v_0 y_0}. \quad (100)$$

By substituting for  $v_c$  and  $v_0$  using equations (24) and (53), respectively, and setting  $J = \dot{M}/(\pi r_0^2)$ , we can obtain the alternative form

$$\beta = \frac{\pi r_0^2 \sigma T_0^4 R_*}{6y_0(1-y_0)GM_*\dot{M}}, \quad (101)$$

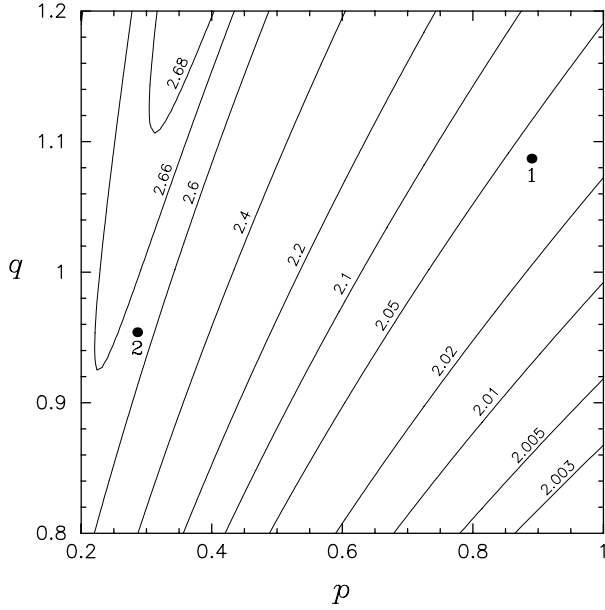


FIG. 6.—Contour plot of the high-energy power-law photon spectral index  $\alpha_0$  as a function of the similarity variables  $p$  and  $q$ , which are related to the fundamental physical parameters  $r_0$ ,  $T_0$ , and  $\dot{M}$  via eq. (104). The value of  $\alpha_0$  is indicated for each curve, and we have set  $R_* = 10$  km and  $M_* = 1.4 M_\odot$ . The parameters used for models 1 and 2 are represented by the labeled points.

or, equivalently,

$$\beta = \frac{2.24 \times 10^{-3}}{y_0(1-y_0)} \left( \frac{R_*}{10 \text{ km}} \right) \left( \frac{M_*}{M_\odot} \right)^{-1} \times \left( \frac{\dot{M}}{10^{16} \text{ g s}^{-1}} \right)^{-1} \left( \frac{r_0}{1 \text{ km}} \right)^2 \left( \frac{T_0}{10^7 \text{ K}} \right)^4. \quad (102)$$

Taken together, equations (95) and (102) allow the determination of the two dimensionless model parameters  $y_0$  and  $\beta$  in terms of  $R_*$ ,  $M_*$ ,  $r_0$ ,  $T_0$ , and  $\dot{M}$ . This closes the system and facilitates the calculation of the emergent photon number spectrum  $\dot{N}_\epsilon$  using equation (86) and the calculation of the column-integrated spectrum  $\Phi_\epsilon$  using equation (89). The values of the parameters  $r_0$ ,  $T_0$ , and  $\dot{M}$  can therefore be extracted by comparing the theoretically predicted photon count rate distributions with X-ray pulsar spectral data.

### 5.3. Similarity Variables

The eigenvalues  $\lambda_n$  are functions of the dimensionless parameters  $y_0$  and  $\beta$ . Based on the dependencies of these parameters on  $r_0$ ,  $T_0$ , and  $\dot{M}$  expressed by equations (95) and (102), we note that the eigenspectrum *remains unchanged* if  $r_0$ ,  $T_0$ , and  $\dot{M}$  are simultaneously varied according to the prescription

$$r_0 \propto T_0^{-9/2} \propto \dot{M}^{9/10}. \quad (103)$$

In this case, the column-integrated Green's function (eq. [81]) also remains unchanged since it depends only on the values of  $\beta$  and  $y_0$ . These findings suggest that it is useful to introduce the new “similarity variables”  $p$  and  $q$ , defined by

$$p \equiv \left( \frac{T_0}{10^7 \text{ K}} \right) \left( \frac{\dot{M}}{10^{16} \text{ g s}^{-1}} \right)^{1/5}, \quad q \equiv \left( \frac{T_0}{10^7 \text{ K}} \right) \left( \frac{r_0}{1 \text{ km}} \right)^{2/9}. \quad (104)$$

In terms of these parameters, equations (95) and (102) for  $y_0$  and  $\beta$  now become

$$y_0 = 1 - 8.57 \times 10^{-4} \left( \frac{R_*}{10 \text{ km}} \right)^{1/2} \left( \frac{M_*}{M_\odot} \right)^{-1/2} p^5 q^{-27/4} \quad (105)$$

and

$$\beta = \frac{2.24 \times 10^{-3}}{y_0(1-y_0)} \left( \frac{R_*}{10 \text{ km}} \right) \left( \frac{M_*}{M_\odot} \right)^{-1} p^{-5} q^9. \quad (106)$$

The introduction of the new variables  $p$  and  $q$  is convenient because it reduces the dimensionality of the parameter space that determines the eigenvalues  $\lambda_n$  from the three-dimensional domain  $(r_0, T_0, \dot{M})$  to the two-dimensional space  $(p, q)$ . In Figure 6 we plot the spectral index  $\alpha_0 = \lambda_0 - 2$  of the photon count rate spectrum as a function of  $p$  and  $q$ , where  $\lambda_0$  is the first eigenvalue and we have set  $R_* = 10$  km and  $M_* = 1.4 M_\odot$  (the same quantity was plotted as a function of  $y_0$  and  $\beta$  in Fig. 2). Note that when  $q$  is increased for a fixed value of  $p$ , the values of  $y_0$  and  $\beta$  both increase according to equations (105) and (106). The source therefore moves farther downstream, and the absorption at the source location becomes stronger. This causes the spectrum to steepen as we move upward along a vertical line in Figure 6. However, if  $q$  becomes very large, the spectrum starts to harden again due to the increasing amount of compression experienced as the source approaches the base of the accretion column.

### 5.4. Example Spectra

Our primary goal in this paper is to explore the effect of bulk Comptonization on the shape of the X-ray continuum spectrum emerging from a pulsar accretion column. The development of complete models that include additional effects such as thermal Comptonization, cyclotron processes, free-free emission and absorption, and iron line formation will be pursued in future work. Here we compare spectra computed using our simplified model with the observations for a few sources in order to focus attention on the role of the accretion shock in the formation of the X-ray continuum. In Figures 7 and 8 we plot the position-dependent

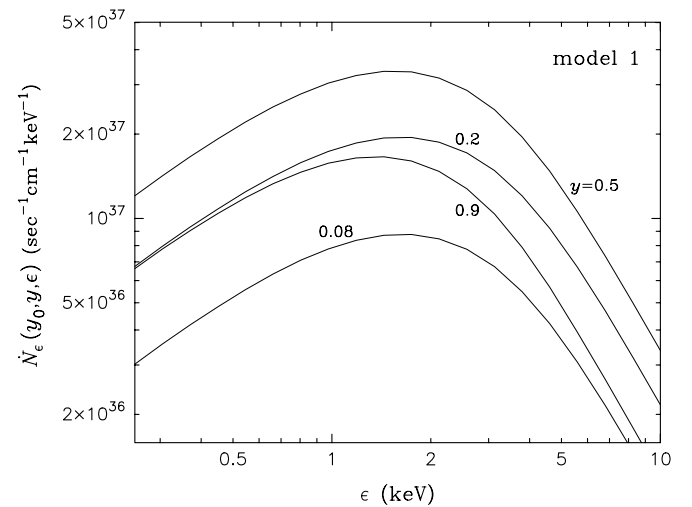


FIG. 7.—Escaping photon distribution  $\dot{N}_\epsilon(y_0, y, \epsilon)$  (eq. [86]) divided by  $(\sigma_{\parallel}/\sigma_{\perp})^{1/2}$  plotted as a function of  $\epsilon$  for the indicated values of  $y$ . These results were computed using the model 1 parameters and describe the spectrum emitted per unit length of the accretion column due to the bulk Comptonization of blackbody radiation.

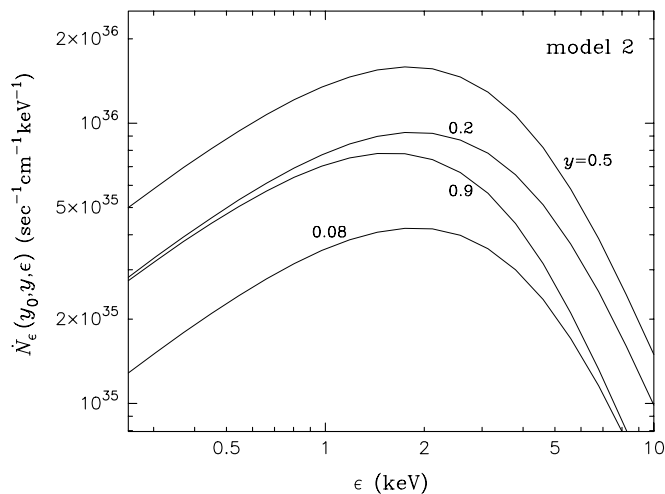


FIG. 8.—Same as Fig. 7, except the results were computed using the model 2 parameters.

photon count rate spectra  $\dot{N}_\epsilon$  (eq. [86]) escaping from the accretion column computed using the two sets of model parameters listed in Table 1. These results were obtained using 20 eigenvalues and eigenfunctions, which yield extremely high precision due to the rapid convergence of the expansion. The theoretical spectra describe the upscattering of Planckian seed photons injected into the base of the accretion column from the surface of the thermal mound. In both cases we use  $M_* = 1.4 M_\odot$  and  $R_* = 10$  km for the stellar mass and radius, respectively. For model 1 (Fig. 7), the parameters adopted are  $r_0 = 6$  km,  $T_0 = 7.3 \times 10^6$  K, and  $\dot{M} = 2.69 \times 10^{16}$  g s $^{-1}$ . In model 2 (Fig. 8) we set  $r_0 = 1.3$  km,  $T_0 = 9.0 \times 10^6$  K, and  $\dot{M} = 3.23 \times 10^{13}$  g s $^{-1}$ . We use equations (104), (105), and (106) to compute the theoretical parameters  $p$ ,  $q$ ,  $y_0$ , and  $\beta$  based on the selected values for  $r_0$ ,  $T_0$ , and  $\dot{M}$ . In model 1 we obtain  $\beta = 26.4505$  and  $y_0 = 0.99977$ , and in model 2 we find that  $\beta = 2.894 \times 10^5$  and  $y_0 = 0.999998$ . Additional parameters are provided in Table 1. The fact that the thermal mound location  $y_0$  is extremely close to unity in both cases indicates that the mound lies just above the surface of the star, as expected. It is interesting to compute the actual physical distance between the thermal mound and the stellar surface,  $h_0$ , which is given by equation (98). Using the parameters corresponding to models 1 and 2 yields  $h_0 = 39.84(\sigma_\perp/\sigma_\parallel)^{1/2}$  cm and  $h_0 = 0.075(\sigma_\perp/\sigma_\parallel)^{1/2}$  cm, respectively. Note that in model 2 the thermal mound is essentially on the surface of the star, whereas in model 1 there is a much larger separation. This reflects the fact that the accretion rate in model 1 is over 800 times larger than in model 2.

The results obtained for the first eigenvalue and for the photon index in model 1 are  $\lambda_0 = 4.0398$  and  $\alpha_0 = 2.0398$ , respectively. In model 2, we find that the spectrum is significantly steeper, with  $\lambda_0 = 4.6382$  and  $\alpha_0 = 2.6382$ . The steeper spectrum obtained in model 2 results from the large value for  $\beta$ , as indicated in Table 1. In general, the escaping spectrum has a

power-law shape at high energies, as expected for a Fermi process, and a low-energy turnover due to the Planck distribution of the seed photons. Note that the emitted radiation is concentrated in a layer just above the thermal mound location, around  $y \sim 0.5$ . This reflects the fact that advection due to collisions with the infalling stream of high-speed electrons tends to keep the photons trapped at low altitudes in the column, and therefore few of them are able to escape through the column walls for  $y \ll 1$ . Since the spin axis and the column axis are not aligned in pulsars, the portion of the accretion column visible along the line of sight to the Earth changes as the pulsar rotates. When combined with the vertical variation of the energy dependence of the escaping photon distribution, this effect will produce a pulse-phase dependence in the observed X-ray spectrum.

In Figures 9 and 10 we plot the theoretical predictions for the phase-averaged photon count rate flux measured at Earth,

$$F_\epsilon(\epsilon) \equiv \frac{\Phi_\epsilon(y_0, \epsilon)}{4\pi D^2}, \quad (107)$$

computed using models 1 and 2, respectively, where  $D$  is the distance to the source and the column-integrated spectrum  $\Phi_\epsilon(y_0, \epsilon)$  is evaluated using equation (89). Also included in Figures 9 and 10 for comparison are plots of the unfolded phase-averaged spectra for the X-ray pulsars 4U 1258–61 (GX 304–1) and 4U 0352+30 (X Persei), respectively. The 4U 1258–61 data were reported by White et al. (1983), and the 4U 0352+30 data are the result of XSPEC analysis of an archival *RXTE* observation taken in 1998 July and reported by Delgado-Martí et al. (2001). Based on estimates from Negueruela (1998), the values adopted for the distance  $D$  are 2.5 kpc for 4U 1258–61 and 0.35 kpc for 4U 0352+30. The observational data represent the deconvolved (incident) spectra, which depend weakly on the detector response model. The theoretical spectra were computed using 20 eigenvalues and eigenfunctions for high accuracy, and various amounts of interstellar absorption were included as indicated in the figures.

Although the results presented here are not fits to the data, we note that the general shape of the pulsar spectrum predicted by the theory agrees fairly well with the observations in each case, including both the turnover at low energies and the power law at higher energies. Several other sources yield similar agreement. In our model, the turnover at  $\sim 2$  keV is due to Planckian photons that escape from the accretion column without experiencing many scatterings. This effect will tend to reduce the amount of absorption required to fit the observational data, compared with the amount required using the standard ad hoc models usually employed in X-ray pulsar spectral analysis (see the discussion in Hickox et al. 2004).

The second source, X Persei, presents an interesting test for the model due to its relatively low luminosity,  $L_X \sim 10^{34}$  ergs s $^{-1}$ . The agreement between the theory and the observations suggests that radiation pressure may still be playing an important role in the dynamics of this source, despite its low luminosity. In

TABLE 1  
MODEL PARAMETERS

Model	$r_0$ (km)	$T_0$ (K)	$\dot{M}$ (g s $^{-1}$ )	$p$	$q$	$y_0$	$\beta$	$\alpha_0$	$h_0/x_{st}$	$v_0/c$
1.....	6.0	$7.3 \times 10^6$	$2.69 \times 10^{16}$	0.890	1.087	0.999770	$2.645 \times 10^1$	2.0398	$2.71 \times 10^{-4}$	$1.48 \times 10^{-4}$
2.....	1.3	$9.0 \times 10^6$	$3.23 \times 10^{13}$	0.286	0.954	0.999998	$2.894 \times 10^5$	2.6382	$2.36 \times 10^{-6}$	$1.22 \times 10^{-6}$

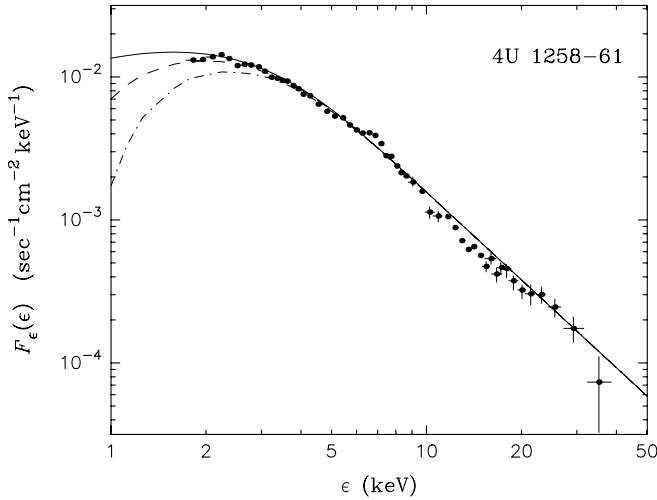


FIG. 9.—Theoretical column-integrated count rate spectrum  $F_\epsilon(\epsilon)$  (eq. [107]) computed using the model 1 parameters along with various amounts of interstellar absorption, compared with the X-ray spectrum of 4U 1258–61. The column densities used are  $N_{\text{H}} = 0$  (solid line),  $3 \times 10^{21}$  (dashed line), and  $9 \times 10^{21} \text{ cm}^{-2}$  (dot-dashed line). The other parameters for the theoretical model are given in Table 1.

this connection, Langer & Rappaport (1982) pointed out that radiation pressure may have a strong effect on the flow dynamics of low-luminosity pulsars if the photon energies are close to the cyclotron resonance, which greatly increases the electron scattering cross section. Furthermore, the dynamical importance of the gas pressure in this luminosity range may lead to the development of a gas-mediated “subshock” within the overall gradual compression of the radiation-dominated shock. This type of hybrid shock is analogous to the “two-fluid” model of cosmic-ray mediated supernova shocks (e.g., Drury & Völk 1981). It is known that in the cosmic-ray case, multiple flow solutions can occur for the same set of upstream boundary conditions (e.g., Becker & Kazanas 2001). There is some possibility that the same type of multistate behavior may occur in X-ray pulsars, which could have interesting observational implications.

## 6. MODEL SELF-CONSISTENCY

The analytical approach employed in this paper is based on the conservation of energy and momentum in the radiation-dominated flow. This leads to the self-consistent determination of the thermal mound location,  $x_0$ , for given values of the fundamental parameters  $r_0$ ,  $T_0$ , and  $\dot{M}$ , as discussed in § 5.1. In this section we verify that the model satisfies the self-consistency conditions required for global energy conservation. We also examine the implications of the one-dimensional escape probability formalism that has been utilized to model the emission of radiation from the column.

### 6.1. Pressure Distribution

The exact dynamical solution for the radiation pressure inside the pulsar accretion column is given by equation (29), which states that

$$P(x) = \frac{7}{4} J v_c \left( \frac{7}{3} \right)^{-1+x/x_{\text{st}}}, \quad (108)$$

where  $x_{\text{st}}$  is the distance between the sonic point and the stellar surface, given by equation (21). In principle, the radiation pressure can also be computed by integrating the particular

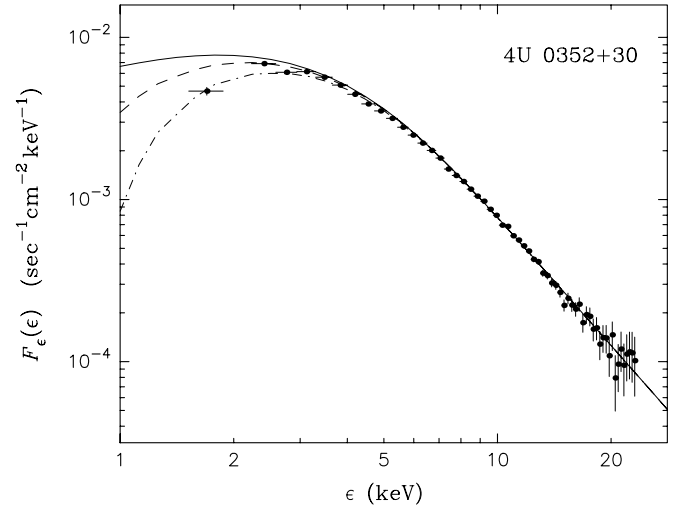


FIG. 10.—Same as Fig. 9, except the data correspond to 4U 0352+30 and the theoretical spectra were computed based on model 2. The column densities used are  $N_{\text{H}} = 0$  (solid line),  $3 \times 10^{21}$  (dashed line), and  $9 \times 10^{21} \text{ cm}^{-2}$  (dot-dashed line).

solution for the photon distribution  $f$  inside the accretion column. Since  $P = U/3$ , we can use equation (32) to write

$$P(x) = \frac{1}{3} \int_0^\infty \epsilon^3 f(x_0, x, \epsilon) d\epsilon, \quad (109)$$

where  $f$  is computed using the convolution (see eq. [44])

$$f(x_0, x, \epsilon) = \int_0^\epsilon \frac{f_G(x_0, x, \epsilon_0, \epsilon)}{N_0} \epsilon_0^2 S(\epsilon_0) d\epsilon_0. \quad (110)$$

Here the blackbody source  $S(\epsilon_0)$  is given by equation (35) and the Green’s function  $f_G$  is evaluated using equation (68), bearing in mind that the quantities  $(x, x_0)$  and  $(y, y_0)$  are interchangeable via equations (47) and (52).

We can check the accuracy of the entire solution technique, including the determination of the eigenfunctions and the eigenvalues, by comparing the exact dynamical result for  $P$  with that obtained by integrating the spectrum. In Figure 11 we plot the exact analytical solution for the radiation pressure computed using equation (108) along with the results obtained by integrating the model 1 and 2 spectra using equation (109). Note that the agreement between the various solutions for  $P$  is excellent, and in each case the pressure achieves the correct stagnation value  $P_{\text{st}} = (7/4) J v_c$  (eq. [30]) as the gas approaches the stellar surface. The agreement between the various results for the pressure confirms that our solution for the radiation spectrum is consistent with the dynamics of the accretion flow.

### 6.2. Total Luminosity

In order to further explore the self-consistency of the formalism developed here, we have also computed the total X-ray luminosity,  $L_X$ , emerging from the column by integrating the escaping number spectrum  $\Phi_\epsilon$  (eq. [87]) using

$$L_X = \int_0^\infty \epsilon \Phi_\epsilon(x_0, \epsilon) d\epsilon. \quad (111)$$

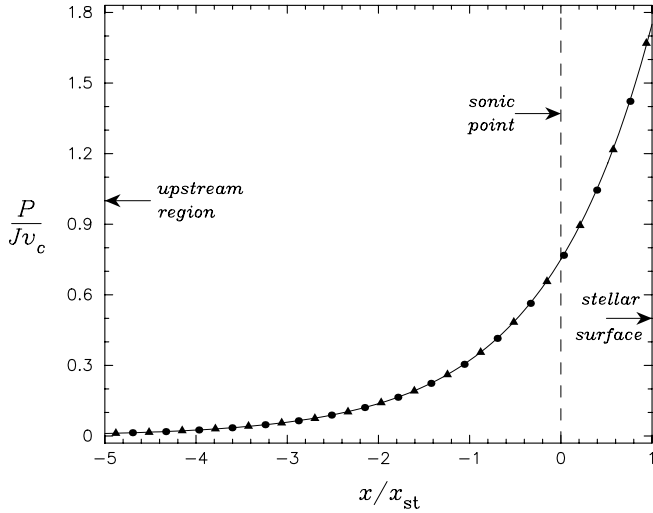


FIG. 11.—Radiation pressure  $P$  plotted in units of  $Jv_c$  as a function of  $x$ , which is the distance measured from the sonic point in the direction of the flow. The dashed vertical line at  $x = 0$  represents the sonic point, and  $x = x_{st}$  at the stellar surface. The exact dynamical solution (eq. [108]) is denoted by the solid line, and the filled circles and triangles represent the values obtained using eq. (109) to integrate the model 1 and 2 spectra, respectively. At the surface of the star, the pressure approaches the stagnation value (eq. [30]) as expected.

We have confirmed that the values obtained using this expression agree precisely with the accretion luminosity given by

$$L_X = \frac{GM_*\dot{M}}{R_*}. \quad (112)$$

The calculations performed in this section and in § 6.1 validate our entire solution procedure for the determination of the radiation spectrum by demonstrating that our results are fully consistent with global energy conservation.

### 6.3. Escape Probability Formalism

Within the context of our one-dimensional model, the diffusion of radiation through the walls of the accretion column is treated in an approximate manner using an escape probability formalism. In this approach, the probability per unit time that a randomly selected photon at location  $x$  inside the column will escape through the walls is equal to  $t_{\text{esc}}^{-1}$ , where the mean escape time  $t_{\text{esc}}$  is a function of  $x$  given by (see eq. [12])

$$t_{\text{esc}}(x) = \frac{r_0^2 \sigma_{\perp} n_e(x)}{c}, \quad (113)$$

with  $r_0$  and  $\sigma_{\perp}$  denoting the radius of the cylindrical column and the electron scattering cross section for photons propagating perpendicular to the column axis, respectively. The escape of radiation through the walls of the accretion column can therefore be modeled approximately using a term of the form

$$\left. \frac{\partial f}{\partial t} \right|_{\text{approx}} = -\frac{f}{t_{\text{esc}}}, \quad (114)$$

which is incorporated into the transport equation (31).

From a technical point of view, the utilization of the escape probability formalism implies that the distribution of the photon number density across the column is proportional to the first eigenfunction of the operator describing the diffusion of radia-

tion perpendicular to the column axis (e.g., Sunyaev & Titarchuk 1980). In a comprehensive, multidimensional calculation, the diffusion of photons perpendicular to the column axis is treated by replacing the escape probability term  $\partial f/\partial t = -f/t_{\text{esc}}$  in the transport equation (31) with the more rigorous expression

$$\left. \frac{\partial f}{\partial t} \right|_{\text{exact}} = \frac{1}{r} \frac{\partial}{\partial r} \left( \frac{cr}{3n_e \sigma_{\perp}} \frac{\partial f}{\partial r} \right), \quad (115)$$

where  $r$  is the radial coordinate measured from the central axis of the cylindrical accretion column. If the gas density is constant across the column at a given height, as assumed here, then equation (115) can be separated to obtain for the first eigenfunction the solution

$$f(r, t) = A \exp\left(-\frac{c\xi^2 t}{3\ell_{\perp}}\right) J_0\left(\frac{\xi r}{\ell_{\perp}}\right), \quad (116)$$

where  $A$  is a constant,  $\xi$  denotes the first eigenvalue,  $J_0$  represents the zeroth-order Bessel function, and

$$\ell_{\perp} \equiv (n_e \sigma_{\perp})^{-1} \quad (117)$$

is the electron scattering mean free path for photons propagating perpendicular to the column axis.

The value of  $\xi$  is determined by satisfying the flux boundary condition at the surface of the column. By employing the Eddington approximation, we can write the boundary condition as

$$\ell_{\perp} \left. \frac{\partial f}{\partial r} \right|_{r=r_0} + \gamma f = 0, \quad (118)$$

where  $\gamma$  is a positive constant of order unity and we have assumed that no radiation is incident on the column from the outside. The precise value of  $\gamma$  is somewhat arbitrary, with Rybicki & Lightman (1979) setting  $\gamma = 3^{1/2}$  and Sunyaev & Titarchuk (1980) setting  $\gamma = 3/2$ . Combining equations (116) and (118), we find that  $\xi$  is the smallest positive root of the equation

$$J_0\left(\frac{\xi r_0}{\ell_{\perp}}\right) = \left(\frac{\xi}{\gamma}\right) J_1\left(\frac{\xi r_0}{\ell_{\perp}}\right), \quad (119)$$

where  $J_1$  denotes the order-unity Bessel function.

The rate of change of the first eigenfunction (eq. [116]) is given by

$$\frac{\partial f}{\partial t} = -\frac{c\xi^2}{3\ell_{\perp}} f(r, t). \quad (120)$$

Comparison of equations (114) and (120) reveals that the escape probability approximation and the rigorous diffusion model yield the same result for the logarithmic time derivative  $\partial \ln f/\partial t$  if the mean escape time  $t_{\text{esc}}$  and the first eigenvalue  $\xi$  are related via

$$t_{\text{esc}} = \frac{3\ell_{\perp}}{c\xi^2}. \quad (121)$$

This equation is well satisfied in all of our sample calculations, which suggests that the escape probability formalism provides a reasonable description of the leakage of photons from the accretion column.

## 7. CONCLUSIONS

We have shown that the simplified model considered here, comprising a radiation-dominated accretion column with a blackbody source/sink at its base and a radiative shock, is able to reproduce the power-law continuum spectra observed in accretion-powered X-ray pulsars with a range of luminosities, as indicated in Figures 9 and 10. Our results represent the first *ab initio* calculations of the X-ray spectrum associated with the physical accretion scenario first suggested by Davidson (1973). For given values of the stellar mass  $M_*$  and the stellar radius  $R_*$ , our model has only three free parameters, namely, the column radius  $r_0$ , the temperature at the top of the thermal mound  $T_0$ , and the accretion rate  $\dot{M}$ . We have confirmed that the solution obtained for the radiation spectrum is consistent with the dynamics of the flow in the accretion column (see Fig. 11). Many pulsars are found to have spectra that are well fitted using a combination of a power law plus a blackbody component, but until now this form has been adopted in a purely *ad hoc* manner. The new model described here finally provides a firm theoretical foundation for this empirical result. Our analytical solution, based on a rigorous eigenfunction expansion, is relatively straightforward to implement computationally because it avoids numerical integration of the transport equation. The work presented here therefore represents a significant step in the development of a comprehensive theory for the spectral formation process in X-ray pulsars.

The photon spectral index  $\alpha_0$  is related to the first eigenvalue  $\lambda_0$  via  $\alpha_0 = \lambda_0 - 2$ , and therefore the leading eigenvalue determines the slope of the high-energy portion of the X-ray spectrum. The value of  $\alpha_0$  is quite sensitive to the strength of the absorption at the thermal mound, which is determined by the parameter  $\beta$ . According to equation (102),  $\beta$  in turn is a strong function of the mound temperature  $T_0$ . The higher the temperature, the stronger the emission and absorption at the blackbody surface of the mound. Model 2 has a higher temperature than model 1, and therefore the value of  $\beta$  is larger. Hence, the spectrum is steeper in model 2 because the photons spend less time on average upscattering in the flow before either escaping through the column walls or being “recycled” by absorption at the mound location. Acceptable values for  $\alpha_0$ , in the range between 2 and 4, are obtained for reasonable source parameters, as indicated in Figures 2 and 6. Although a broad range of spectral indices can be produced, we must have  $\alpha_0 > 2$  in order to avoid an infinite photon energy density since the model considered here does not include a high-energy cutoff.

The shape of the Green’s function spectrum derived here is qualitatively similar to the results obtained using the “bulk motion Comptonization” model coded into the XSPEC package using the BMC function (see Shrader & Titarchuk 1998, 1999; Borozdin et al. 1999). The BMC model includes parameters corresponding to the high-energy spectral index, the temperature of the soft photon source, the fraction of the Comptonized component in the resulting spectrum, and the size of the emitting region. However, the BMC model is designed to treat spectral formation in black hole accretion flows, whereas our focus here

is on neutron star accretion. Hence, the model developed in this paper can be viewed as a parallel formalism that is optimized for the treatment of the spectral formation process in accretion-powered X-ray pulsars. In this sense, our theory translates the free parameters of a generalized bulk Comptonization model into specific values for the accretion rate, temperature, and column radius for a particular X-ray pulsar.

Our goal in this paper is to explore the direct role of the accretion shock in producing the observed continuum spectra in X-ray pulsars via the first-order Fermi process. Although the model produces spectra that are quite similar to those observed from several X-ray pulsars, it cannot explain the spectra from other sources. For example, the observed spectra for several of the brightest pulsars with luminosities in the range  $10^{37}$ – $10^{38}$  ergs s<sup>-1</sup> (e.g., Her X-1) are very flat power laws leading up to a sharp exponential cutoff. The photon index in these sources is typically  $\alpha_0 \sim 1$ , which is outside the range allowed by our model since it does not include a high-energy cutoff. In order to understand spectral formation in the brightest pulsars, additional effects such as thermal Comptonization, cyclotron features, bremsstrahlung, and iron emission must be incorporated into the model. In principle, one should also consider higher order relativistic effects that can alter the form of the fundamental transport equation (Psaltis & Lamb 1997). Thermal Comptonization is particularly important since this process redistributes energy from the highest frequency photons to lower energies via electron recoil. This naturally leads to the development of a high-energy exponential turnover and a concomitant flattening of the spectrum at moderate energies, as observed.

The thermal Comptonization process was studied by Lyubarskii & Sunyaev (1982) and Becker (1988) in the context of plane-parallel shocks. However, the velocity profiles employed by these authors are not consistent with the structure of an X-ray pulsar accretion column. Poutanen & Gierliński (2003) computed X-ray pulsar spectra based on the thermal Comptonization of soft radiation in a hot layer above the magnetic pole, but their model did not include a complete treatment of the bulk process, which is of crucial importance in X-ray pulsars. In this paper we have carefully analyzed the effect of bulk Comptonization on the emitted spectrum, while neglecting the corresponding thermal process. The inclusion of thermal Comptonization is beyond the scope of the present paper because it renders the transport equation insoluble via analytical means. However, in future work we intend to develop a comprehensive numerical model that incorporates both the bulk and thermal processes.

The authors would like to thank Lev Titarchuk, Philippe Laurent, and Nikos Kylafis, who provided useful comments on the manuscript. The authors are also grateful to the anonymous referee, whose careful reading and stimulating suggestions led to significant improvements in the paper. P. A. B. would also like to acknowledge generous support provided by the Office of Naval Research.

## APPENDIX A

## FUNDAMENTAL SOLUTION IN THE DOWNSTREAM REGION

When  $y \neq y_0$ , the spatial separation functions  $g(\lambda, y)$  satisfy the homogeneous differential equation (cf. eq. [55])

$$y(1-y)\frac{d^2g}{dy^2} + \left(\frac{1-5y}{4}\right)\frac{dg}{dy} + \left(\frac{\lambda y + y - 1}{4y}\right)g = 0, \quad (\text{A1})$$

which has the fundamental solutions

$$\varphi_1(\lambda, y) \equiv yF(a, b; c; y), \tag{A2}$$

$$\varphi_1^*(\lambda, y) \equiv y^{-1/4}F(a - 5/4, b - 5/4; 2 - c; y), \tag{A3}$$

where  $F(a, b; c; z)$  denotes the hypergeometric function (Abramowitz & Stegun 1970) and we have made the definitions

$$a \equiv \frac{9 - \sqrt{17 + 16\lambda}}{8}, \quad b \equiv \frac{9 + \sqrt{17 + 16\lambda}}{8}, \quad c \equiv \frac{9}{4}. \tag{A4}$$

As explained in the discussion following equation (61), in the downstream limit the radiation pressure approaches the finite stagnation value given by equation (30). The spatial separation functions  $g(\lambda, y)$  should mimic this behavior, and therefore we require that  $g$  approaches a constant in the limit  $y \rightarrow 1$ . This does not happen in general, but only if the separation constant  $\lambda$  is equal to one of the eigenvalues  $\lambda_n$ , in which case we obtain the eigenfunction

$$g_n(y) \equiv g(\lambda_n, y). \tag{A5}$$

The hypergeometric functions appearing in equations (A2) and (A3) can be evaluated at  $y = 1$  using equation (15.1.20) from Abramowitz & Stegun (1970), which gives for general values of  $a, b$ , and  $c$

$$F(a, b; c; 1) = \frac{\Gamma(c)\Gamma(c - a - b)}{\Gamma(c - a)\Gamma(c - b)}. \tag{A6}$$

However, for the values of  $a, b$ , and  $c$  in the current application, we find that

$$c - a - b = 0, \tag{A7}$$

and therefore the hypergeometric functions  $F(a, b; c; y)$  and  $F(a - 5/4, b - 5/4; 2 - c; y)$  each *diverge* in the downstream limit  $y \rightarrow 1$ .

Based on the asymptotic behaviors of the hypergeometric functions appearing in the expressions for  $\varphi_1$  and  $\varphi_1^*$ , we conclude that in the downstream region ( $y \geq y_0$ ), the eigenfunction  $g_n$  must be represented by a suitable linear combination of  $\varphi_1$  and  $\varphi_1^*$  that remains finite as  $y \rightarrow 1$ . In order to make further progress, we need to employ equation (15.3.10) from Abramowitz & Stegun (1970), which yields for general  $a, b$ , and  $y$

$$F(a, b; a + b; y) = \frac{\Gamma(a + b)}{\Gamma(a)\Gamma(b)} \sum_{n=0}^{\infty} \frac{(a)_n (b)_n}{(n!)^2} [2\Psi(n + 1) - \Psi(a + n) - \Psi(b + n) - \ln(1 - y)](1 - y)^n, \tag{A8}$$

where

$$\Psi(z) \equiv \frac{1}{\Gamma(z)} \frac{d\Gamma(z)}{dz}. \tag{A9}$$

By making use of this expression, we note that the logarithmic divergences of the two functions  $\varphi_1$  and  $\varphi_1^*$  in the limit  $y \rightarrow 1$  can be balanced by creating the new function

$$\varphi_2(\lambda, y) \equiv \frac{\Gamma(b)}{\Gamma(c)\Gamma(1 - b)} \varphi_1(\lambda, y) - \frac{\Gamma(1 - a)}{\Gamma(2 - c)\Gamma(a)} \varphi_1^*(\lambda, y), \tag{A10}$$

which remains finite as  $y \rightarrow 1$ . Hence,  $\varphi_2$  represents the fundamental solution for  $g_n$  in the region downstream from the thermal mound located at  $y = y_0$ . We can use the asymptotic behaviors of  $\varphi_1$  and  $\varphi_1^*$  as  $y \rightarrow 1$  to conclude that

$$\lim_{y \rightarrow 1} \varphi_2(\lambda, y) = \frac{\pi[\cot(\pi a) + \cot(\pi b)]}{\Gamma(a)\Gamma(1 - b)}. \tag{A11}$$

Since the solutions  $\varphi_1$  and  $\varphi_2$  are applicable in the upstream and downstream regions, respectively, the global expression for the eigenfunction  $g_n$  is therefore

$$g_n(y) = \begin{cases} \varphi_1(\lambda_n, y), & y \leq y_0, \\ B_n \varphi_2(\lambda_n, y), & y \geq y_0, \end{cases} \tag{A12}$$

where the constant  $B_n$  is evaluated using the continuity condition

$$B_n = \frac{\varphi_1(\lambda_n, y_0)}{\varphi_2(\lambda_n, y_0)}. \tag{A13}$$

It follows from equations (A11), (A12), and (A13) that the downstream value of  $g_n$  is given by

$$\lim_{y \rightarrow 1} g_n(y) = \frac{\pi[\cot(\pi a) + \cot(\pi b)]}{\Gamma(a)\Gamma(1-b)} \frac{\varphi_1(\lambda_n, y_0)}{\varphi_2(\lambda_n, y_0)}, \tag{A14}$$

where  $a$  and  $b$  are evaluated using equation (61).

### APPENDIX B

#### ANALYTICAL EXPRESSION FOR THE WRONSKIAN

The derivation of the eigenvalue equation (67) in § 4.2 makes use of the Wronskian of the two functions  $\varphi_1$  and  $\varphi_2$ , defined by

$$W(\lambda, y) \equiv \varphi_1 \frac{d\varphi_2}{dy} - \varphi_2 \frac{d\varphi_1}{dy}. \tag{B1}$$

It is useful to derive an analytical expression for  $W$  based on the differential equation (55) governing the two functions  $\varphi_1$  and  $\varphi_2$ , which can be rewritten in the self-adjoint form

$$\frac{d}{dy} \left[ y^{1/4}(1-y) \frac{d\varphi}{dy} \right] + \frac{\lambda}{4y^{3/4}} \varphi - T\varphi = 0, \tag{B2}$$

where

$$T \equiv \frac{1-y}{4y^{7/4}} + \frac{3\beta v_0 \delta(y-y_0)}{7v_c y^{3/4}}. \tag{B3}$$

By applying equation (B2) to the function  $\varphi_2$  and multiplying the result by  $\varphi_1$ , and then subtracting from this the same expression with  $\varphi_1$  and  $\varphi_2$  interchanged, we obtain

$$\varphi_1 \frac{d}{dy} \left[ y^{1/4}(1-y) \frac{d\varphi_2}{dy} \right] - \varphi_2 \frac{d}{dy} \left[ y^{1/4}(1-y) \frac{d\varphi_1}{dy} \right] = 0, \tag{B4}$$

which can be rewritten as

$$y^{1/4}(1-y) \frac{dW}{dy} + W \frac{d}{dy} \left[ y^{1/4}(1-y) \right] = 0, \tag{B5}$$

where we have made use of the result

$$\frac{dW}{dy} = \varphi_1 \frac{d^2\varphi_2}{dy^2} - \varphi_2 \frac{d^2\varphi_1}{dy^2}. \tag{B6}$$

Equation (B5) can be rearranged in the form

$$\frac{d \ln W}{dy} = - \frac{d}{dy} \ln \left[ y^{1/4}(1-y) \right], \tag{B7}$$

which can be integrated to obtain the exact solution

$$W(\lambda, y) = \frac{D(\lambda)}{y^{1/4}(1-y)}, \tag{B8}$$

where  $D(\lambda)$  is an integration constant that may depend on  $\lambda$  but not on  $y$ . The exact dependence of  $D$  on  $\lambda$  can be derived by analyzing the behaviors of the functions  $\varphi_1$  and  $\varphi_2$  in the limit  $y \rightarrow 0$ . For small values of  $y$ , we have the asymptotic expressions (Abramowitz & Stegun 1970)

$$\begin{aligned} \varphi_1 &\rightarrow y, & y &\rightarrow 0, \\ \varphi_2 &\rightarrow -\frac{\Gamma(1-a)}{\Gamma(a)\Gamma(2-c)}y^{-1/4}, & y &\rightarrow 0. \end{aligned} \tag{B9}$$

We therefore find that asymptotically

$$W \rightarrow \frac{5}{4} \frac{\Gamma(1-a)}{\Gamma(a)\Gamma(2-c)}y^{-1/4}, \quad y \rightarrow 0. \tag{B10}$$

Comparing this result with equation (B8), we conclude that

$$D(\lambda) = \frac{5}{4} \frac{\Gamma(1-a)}{\Gamma(a)\Gamma(2-c)}, \tag{B11}$$

and therefore the exact solution for the Wronskian is given by

$$W(\lambda, y) = \frac{5}{4} \frac{\Gamma(1-a)}{\Gamma(a)\Gamma(2-c)} \frac{y^{-1/4}}{1-y}. \tag{B12}$$

This result is used in § 4.2 in the derivation of the eigenvalue equation (67).

### APPENDIX C

#### ORTHOGONALITY OF THE EIGENFUNCTIONS

The calculation of the expansion coefficients  $C_n$  in the series representation for the Green's function

$$f_G(y_0, y, \epsilon_0, \epsilon) = \epsilon^{-3} \sum_{n=0}^{\infty} C_n \left(\frac{\epsilon}{\epsilon_0}\right)^{3-\lambda_n} g_n(y) \tag{C1}$$

discussed in § 4.3 depends on the establishment of the orthogonality of the eigenfunctions  $g_n(y)$ . Here we demonstrate that the eigenfunctions form an orthogonal set as required. Let us suppose that  $g_n(y)$  and  $g_m(y)$  are two eigenfunctions corresponding to the distinct eigenvalues  $\lambda_n$  and  $\lambda_m$ , respectively. The functions  $g_n$  and  $g_m$  satisfy the differential equation (55), and therefore we can utilize the self-adjoint form to write (cf. eq. [B2])

$$g_m \left\{ \frac{d}{dy} \left[ y^{1/4}(1-y) \frac{dg_n}{dy} \right] + \frac{\lambda_n}{4y^{3/4}} g_n - T g_n \right\} = 0 \tag{C2}$$

and

$$g_n \left\{ \frac{d}{dy} \left[ y^{1/4}(1-y) \frac{dg_m}{dy} \right] + \frac{\lambda_m}{4y^{3/4}} g_m - T g_m \right\} = 0, \tag{C3}$$

where  $T$  is given by equation (B3). Subtracting the second equation from the first yields, after integrating by parts with respect to  $y$  from  $y = 0$  to 1,

$$(\lambda_n - \lambda_m) \int_0^1 y^{-3/4} g_n(y) g_m(y) dy = 4y^{1/4}(1-y) \left[ g_n \frac{dg_m}{dy} - g_m \frac{dg_n}{dy} \right] \Big|_0^1. \tag{C4}$$

Based on the asymptotic behaviors of the eigenfunctions  $g_n$  and  $g_m$  given by equations (A14) and (B9), we find that the right-hand side of equation (C4) vanishes exactly, and we therefore obtain

$$(\lambda_n - \lambda_m) \int_0^1 y^{-3/4} g_n(y) g_m(y) dy = 0, \quad n \neq m \tag{C5}$$

which establishes the orthogonality of the eigenfunctions.

## APPENDIX D

## QUADRATIC NORMALIZATION INTEGRALS

The evaluation of the Green's function  $f_G$  using equation (C1) relies on knowledge of the expansion coefficients  $C_n$ , which are given by

$$C_n = \frac{12\dot{N}_0 y_0^{-3/4} g_n(y_0)}{7\pi r_0^2 v_c I_n}, \quad (\text{D1})$$

where the quadratic normalization integrals  $I_n$  are defined by

$$I_n \equiv \int_0^1 y^{-3/4} g_n^2(y) dy. \quad (\text{D2})$$

The direct computation of the normalization integrals  $I_n$  via numerical integration is costly and time consuming, and therefore it is desirable to have an alternative procedure available for their evaluation. In fact, it is possible to derive an analytical expression for the normalization integrals based on manipulation of the fundamental differential equation (55) governing the eigenfunctions  $g_n(y)$ .

Let us suppose that  $g(\lambda, y)$  is a general solution to equation (55) for an arbitrary value of  $\lambda$  (i.e., not necessarily an eigenvalue) that has the asymptotic upstream behavior

$$g(\lambda, y) \rightarrow y, \quad y \rightarrow 0. \quad (\text{D3})$$

We also require that  $g$  be continuous at  $y = y_0$  and that it satisfy the derivative jump condition (see eq. [57])

$$\lim_{\varepsilon \rightarrow 0} \left. \frac{dg}{dy} \right|_{y=y_0+\varepsilon} - \left. \frac{dg}{dy} \right|_{y=y_0-\varepsilon} = \frac{3\beta}{4y_0} g(\lambda, y_0). \quad (\text{D4})$$

After a bit of algebra, we find that the global solution for  $g$  can be expressed as

$$g(\lambda, y) = \begin{cases} \varphi_1(\lambda, y), & y \leq y_0, \\ (1 + \hat{a})\varphi_1(\lambda, y) + \hat{b}\varphi_2(\lambda, y), & y \geq y_0, \end{cases} \quad (\text{D5})$$

where  $\hat{a}$  and  $\hat{b}$  are given by

$$\hat{a} = -\frac{3\beta\varphi_1(\lambda, y_0)\varphi_2(\lambda, y_0)}{4y_0W(\lambda, y_0)}, \quad \hat{b} = \frac{3\beta\varphi_1^2(\lambda, y_0)}{4y_0W(\lambda, y_0)}, \quad (\text{D6})$$

and the Wronskian  $W$  is evaluated using equation (B12).

Comparing the general solution for  $g(\lambda, y)$  with the solution for the eigenfunction  $g_n(y)$  given by equation (A12), we note that

$$\lim_{\lambda \rightarrow \lambda_n} \hat{a} = -1, \quad \lim_{\lambda \rightarrow \lambda_n} \hat{b} = B_n. \quad (\text{D7})$$

We can now use the self-adjoint form of equation (55) to write (cf. eqs. [C2] and [C3])

$$g_n \left\{ \frac{\partial}{\partial y} \left[ y^{1/4}(1-y) \frac{\partial g}{\partial y} \right] + \frac{\lambda}{4y^{3/4}} g - Tg \right\} = 0 \quad (\text{D8})$$

and

$$g \left\{ \frac{d}{dy} \left[ y^{1/4}(1-y) \frac{dg_n}{dy} \right] + \frac{\lambda_n}{4y^{3/4}} g_n - Tg_n \right\} = 0. \quad (\text{D9})$$

Subtracting the second equation from the first and integrating by parts from  $y = 0$  to 1 yields

$$(\lambda - \lambda_n) \int_0^1 y^{-3/4} g(\lambda, y) g_n(y) dy = 4y^{1/4}(1-y) \left[ g(\lambda, y) \frac{dg_n}{dy} - g_n(y) \frac{\partial g}{\partial y} \right] \Big|_0^1. \quad (\text{D10})$$

Since  $g \rightarrow y$  and  $g_n \rightarrow y$  as  $y \rightarrow 0$ , we conclude that the evaluation at the lower bound  $y = 0$  on the right-hand side yields zero, and consequently in the limit  $\lambda \rightarrow \lambda_n$  we obtain for the quadratic normalization integral  $I_n$

$$I_n = \int_0^1 y^{-3/4} g_n^2(y) dy = \lim_{\lambda \rightarrow \lambda_n} \frac{4y^{1/4}(1-y)[g(\lambda, y)(dg_n/dy) - g_n(y)(\partial g/\partial y)]}{\lambda - \lambda_n} \Bigg|_{y=1} . \tag{D11}$$

The numerator and denominator on the right-hand side of equation (D11) each vanish in the limit  $\lambda \rightarrow \lambda_n$ , and therefore we can employ L'Hôpital's rule to show that (e.g., Becker 1997)

$$I_n = \lim_{\lambda \rightarrow \lambda_n} 4y^{1/4}(1-y) \left[ \frac{\partial g}{\partial \lambda} \frac{dg_n}{dy} - g_n \frac{\partial^2 g}{\partial y \partial \lambda} \right] \Bigg|_{y=1} . \tag{D12}$$

Substituting the analytical forms for  $g_n(y)$  and  $g(\lambda, y)$  given by equations (A12) and (D5), respectively, we find that equation (D12) can be rewritten as

$$I_n = \lim_{y \rightarrow 1} 4y^{1/4}(1-y) B_n \left[ W(\lambda, y) \frac{d\hat{a}}{d\lambda} + B_n \frac{\partial \varphi_2}{\partial \lambda} \frac{\partial \varphi_2}{\partial y} - B_n \varphi_2(\lambda, y) \frac{\partial^2 \varphi_2}{\partial y \partial \lambda} \right] \Bigg|_{\lambda=\lambda_n} , \tag{D13}$$

where we have also utilized equations (B1) and (D6). Based on the asymptotic behavior of  $\varphi_2$  given by equation (A11), we conclude that the final two terms on the right-hand side of equation (D13) contribute nothing in the limit  $y \rightarrow 1$ , and therefore our expression for  $I_n$  reduces to

$$I_n = \lim_{y \rightarrow 1} 4y^{1/4}(1-y) B_n W(\lambda, y) \frac{d\hat{a}}{d\lambda} \Bigg|_{\lambda=\lambda_n} . \tag{D14}$$

Since  $y = 1$  is a singular point of the differential equation (55), it is convenient to employ the relation (see eq. [B8])

$$W(\lambda, y)y^{1/4}(1-y) = W(\lambda, y_0)y_0^{1/4}(1-y_0), \tag{D15}$$

which allows us to transform the evaluation in equation (D14) from  $y = 1$  to  $y = y_0$  to obtain the equivalent result

$$I_n = 4y_0^{1/4}(1-y_0)\hat{a}W(\lambda, y_0) \frac{\varphi_1(\lambda_n, y_0)}{\varphi_2(\lambda_n, y_0)} \frac{d \ln \hat{a}}{d\lambda} \Bigg|_{\lambda=\lambda_n} , \tag{D16}$$

where we have also substituted for  $B_n$  using equation (A13). The derivative on the right-hand side can be evaluated using equation (D6), which yields

$$\frac{d \ln \hat{a}}{d\lambda} = \frac{\partial \ln \varphi_1}{\partial \lambda} + \frac{\partial \ln \varphi_2}{\partial \lambda} - \frac{\partial \ln W}{\partial \lambda} , \tag{D17}$$

where the derivative of the Wronskian is given by (see eqs. [A4] and [B12])

$$\frac{\partial \ln W}{\partial \lambda} = \frac{\Psi(a) + \Psi(1-a)}{(17 + 16\lambda)^{1/2}} \tag{D18}$$

and

$$\Psi(z) \equiv \frac{1}{\Gamma(z)} \frac{d\Gamma(z)}{dz} . \tag{D19}$$

Combining equations (D6), (D16), (D17), and (D18), we find that the quadratic normalization integrals can be evaluated using the closed-form expression

$$I_n = K(\lambda_n, y_0), \tag{D20}$$

where

$$K(\lambda, y) \equiv 3\beta y^{-3/4}(1-y)\varphi_1^2(\lambda, y) \left[ \frac{\Psi(a) + \Psi(1-a)}{(17 + 16\lambda)^{1/2}} - \frac{\partial \ln \varphi_1}{\partial \lambda} - \frac{\partial \ln \varphi_2}{\partial \lambda} \right] . \tag{D21}$$

This formula provides an extremely efficient alternative to numerical integration for the computation of  $I_n$ .

APPENDIX E

COLUMN-INTEGRATED GREEN'S FUNCTION

In § 4.5 we demonstrated that the column-integrated Green's function  $\Phi_\epsilon^G(y_0, \epsilon_0, \epsilon)$  can be written as (see eq. [81])

$$\Phi_\epsilon^G(y_0, \epsilon_0, \epsilon) = \frac{\dot{N}_0}{\epsilon y_0^{3/4}} \sum_{n=0}^{\infty} \frac{g_n(y_0)}{I_n} \left(\frac{\epsilon}{\epsilon_0}\right)^{3-\lambda_n} X_n, \tag{E1}$$

where the quadratic normalization integrals  $I_n$  are computed using equation (72) and

$$X_n \equiv \int_0^1 g_n(y)(1-y)y^{-1} dy. \tag{E2}$$

As an alternative to numerical integration for the evaluation of the integral  $X_n$ , here we derive an analytical expression for this quantity. First we use equation (63) to substitute for  $g_n(y)$  in equation (E2) to obtain

$$X_n = \int_0^{y_0} \varphi_1(\lambda_n, y)(1-y) \frac{dy}{y} + \frac{\varphi_1(\lambda_n, y_0)}{\varphi_2(\lambda_n, y_0)} \int_{y_0}^1 \varphi_2(\lambda_n, y)(1-y) \frac{dy}{y}. \tag{E3}$$

Substituting for  $\varphi_2$  using equation (62) and rearranging terms, we can write

$$X_n = L_1 \frac{\varphi_1(\lambda_n, y_0)}{\varphi_2(\lambda_n, y_0)} \int_0^1 \varphi_1(\lambda_n, y)(1-y) \frac{dy}{y} - L_2 \frac{\varphi_1^*(\lambda_n, y_0)}{\varphi_2(\lambda_n, y_0)} \int_0^{y_0} \varphi_1(\lambda_n, y)(1-y) \frac{dy}{y} - L_2 \frac{\varphi_1(\lambda_n, y_0)}{\varphi_2(\lambda_n, y_0)} \int_{y_0}^1 \varphi_1^*(\lambda_n, y)(1-y) \frac{dy}{y}, \tag{E4}$$

where

$$L_1 \equiv \frac{\Gamma(b)}{\Gamma(c)\Gamma(1-b)}, \quad L_2 \equiv \frac{\Gamma(1-a)}{\Gamma(2-c)\Gamma(a)}. \tag{E5}$$

To make further progress, we need to evaluate the fundamental indefinite integrals

$$K_1 \equiv \int \varphi_1(\lambda_n, y)(1-y) \frac{dy}{y}, \quad K_2 \equiv \int \varphi_1^*(\lambda_n, y)(1-y) \frac{dy}{y}. \tag{E6}$$

Fortunately, these integrals can be carried out analytically. By applying equation (15.2.1) from Abramowitz & Stegun (1970) twice, we obtain for  $K_1$  the result

$$K_1 = \frac{(c-1)}{(a-1)(b-1)} \frac{(c-2)}{(a-2)(b-2)} F(a-2, b-2; c-2; y) + \frac{(1-y)(c-1)}{(a-1)(b-1)} F(a-1, b-1; c-1; y) + C_1, \tag{E7}$$

where  $C_1$  is an integration constant. Likewise, we can apply equation (15.2.4) from Abramowitz & Stegun (1970) twice to find that

$$K_2 = \frac{(1-y)y^{2-c}}{2-c} F(1-a, 1-b; 3-c; y) + \frac{y^{3-c}}{(2-c)(3-c)} F(1-a, 1-b; 4-c; y) + C_2, \tag{E8}$$

where  $C_2$  is another integration constant. Combining relations and simplifying, after some algebra we obtain the final result

$$\begin{aligned} X_n = & \frac{\Gamma(1-a)(1-y_0)^2}{\Gamma(a)\varphi_2(\lambda_n, y_0)} \left\{ \frac{y_0^{2-c}\varphi_1(\lambda_n, y_0)}{\Gamma(3-c)} \left[ F(2-a, 2-b; 3-c; y_0) + \frac{y_0}{3-c} F(3-a, 3-b; 4-c; y_0) \right] \right. \\ & + \frac{\varphi_1^*(\lambda_n, y_0)}{(a-1)(b-1)\Gamma(1-c)} \left[ F(a, b; c-1; y_0) + \frac{(c-2)}{(a-2)(b-2)} F(a, b; c-2; y_0) \right] \left. \right\} \\ & + \frac{(1-c)}{(a-1)(b-1)} \left[ 1 + \frac{(c-2)}{(a-2)(b-2)} \right]. \end{aligned} \tag{E9}$$

This formula allows the efficient computation of the integrals  $X_n$  appearing in equation (81) for the column-integrated Green's function.

## REFERENCES

- Abramowitz, M., & Stegun, I. A. 1970, *Handbook of Mathematical Functions* (New York: Dover)
- Basko, M. M., & Sunyaev, R. A. 1975, *A&A*, 42, 311
- . 1976, *MNRAS*, 175, 395
- Becker, P. A. 1988, *ApJ*, 327, 772
- . 1992, *ApJ*, 397, 88
- . 1997, *J. Math. Phys.*, 38, 3692
- . 1998, *ApJ*, 498, 790
- . 2003, *MNRAS*, 343, 215
- Becker, P. A., & Begelman, M. C. 1986, *ApJ*, 310, 534
- Becker, P. A., & Kazanas, D. 2001, *ApJ*, 546, 429
- Becker, P. A., & Wolff, M. T. 2005, *ApJ*, 621, L45
- Blandford, R. D., & Payne, D. G. 1981a, *MNRAS*, 194, 1033
- . 1981b, *MNRAS*, 194, 1041
- Borozdin, K., et al. 1999, *ApJ*, 517, 367
- Burnard, D. J., Aarons, J., & Klein, R. I. 1991, *ApJ*, 367, 575
- Coburn, W., et al. 2002, *ApJ*, 580, 394
- Colpi, M. 1988, *ApJ*, 326, 223
- Davidson, K. 1973, *Nature*, 246, 1
- Delgado-Martí, H., Levine, A. M., Pfahl, E., & Rappaport, S. A. 2001, *ApJ*, 546, 455
- di Salvo, T., Burderi, L., Robba, N. R., & Guainazzi, M. 1998, *ApJ*, 509, 897
- Drury, L. O'C., & Völk, H. J. 1981, *ApJ*, 248, 344
- Giacconi, R., et al. 1971, *ApJ*, 167, L67
- Gleeson, L. J., & Axford, W. I. 1967, *ApJ*, 149, L115
- Harding, A. K. 1994, in *AIP Conf. Proc.* 308, *The Evolution of X-Ray Binaries*, ed. S. S. Holt & C. S. Day (New York: AIP), 429
- . 2003, in *Pulsars, AXPs and SGRs Observed with BeppoSAX and Other Observatories*, ed. G. Cusumano, E. Massaro, & T. Mineo (Rome: Aracne Editrice), 127
- Hickox, R. C., Narayan, R., & Kallman, T. R. 2004, *ApJ*, 614, 881
- Klein, J., et al. 1996, *ApJ*, 457, L85
- Langer, S. H., & Rappaport, S. 1982, *ApJ*, 257, 733
- Laurent, P., & Titarchuk, L. 1999, *ApJ*, 511, 289
- . 2001, *ApJ*, 562, L67
- Lyubarskii, Yu. E., & Sunyaev, R. A. 1982, *Soviet Astron. Lett.*, 8, 330
- Mastichiadis, A., & Kylafis, N. D. 1992, *ApJ*, 384, 136
- Mészáros, P., & Nagel, W. 1985a, *ApJ*, 298, 147
- . 1985b, *ApJ*, 299, 138
- Nagel, W. 1981, *ApJ*, 251, 288
- Negueruela, I. 1998, *A&A*, 338, 505
- Parker, E. N. 1965, *Planet. Space Sci.*, 13, 9
- Payne, D. G., & Blandford, R. D. 1981, *MNRAS*, 196, 781
- Poutanen, J., & Gierliński, M. 2003, *MNRAS*, 343, 1301
- Psaltis, D., & Lamb, F. K. 1997, *ApJ*, 488, 881
- Rybicki, G. B., & Lightman, A. P. 1979, *Radiative Processes in Astrophysics* (New York: Wiley)
- Schneider, P., & Bogdan, T. J. 1989, *ApJ*, 347, 496
- Schneider, P., & Kirk, J. G. 1987, *ApJ*, 323, L87
- Shrader, C. R., & Titarchuk, L. 1998, *ApJ*, 499, L31
- . 1999, *ApJ*, 521, L121
- Skilling, J. 1975, *MNRAS*, 172, 557
- Stawicki, O., Fichtner, H., & Schlickeiser, R. 2000, *A&A*, 358, 347
- Sunyaev, R. A., & Titarchuk, L. G. 1980, *A&A*, 86, 121
- Tananbaum, H., et al. 1972, *ApJ*, 174, L143
- Titarchuk, L., Cui, W., & Wood, K. S. 2002, *ApJ*, 576, L49
- Titarchuk, L., Kazanas, D., & Becker, P. A. 2003, *ApJ*, 598, 411
- Titarchuk, L., Mastichiadis, A., & Kylafis, N. D. 1996, *A&AS*, 120, 171C
- . 1997, *ApJ*, 487, 834
- Titarchuk, L., & Shrader, C. R. 2002, *ApJ*, 567, 1057
- Titarchuk, L., & Zannias, T. 1998, *ApJ*, 493, 863
- Turolla, R., Zane, S., & Titarchuk, L. 2002, *ApJ*, 576, 349
- Wang, Y.-M., & Frank, J. 1981, *A&A*, 93, 255
- White, N. E., Nagase, F., & Parmar, A. N. 1995, in *X-Ray Binaries*, ed. W. H. G. Lewin, J. Van Paradijs, & E. P. J. Van den Heuvel (New York: Cambridge Univ. Press), 1
- White, N. E., Swank, J. H., & Holt, S. S. 1983, *ApJ*, 270, 711
- Yahel, R. Z. 1980, *ApJ*, 236, 911